WILEY-VCH

RESEARCH ARTICLE

Transparent Single-Layer Graphene Electrodes for Deciphering and Enhancing Microbead-Based Electrochemiluminescence Immunoassay

Jialian Ding,[a] Yafeng Wang,[b] Leslie R. Arias-Aranda,[c] Patrick C. Chaumet,[d] Neso Sojic*[c] and Bin Su*[a, e]

[a] J. L. Ding, Prof. Dr. B. Su
State Key Laboratory of Soil Pollution Control and Safety, Zhejiang Key Laboratory of Excited-State Energy Conversion and Energy Storage, Department of Chemistry
Zhejiang University
Hangzhou 310058, China
E-mail: subin@zju.edu.cn

[b] Y. F. Wang
Department of Clinical Laboratory, Sir Run Run Shaw Hospital
Zhejiang University School of Medicine
Hangzhou 310016, China

[c] L. R. Arias-Aranda, Prof. N. Sojic
CNRS, Bordeaux INP, ISM, UMR 5255, ENSMAC
University of Bordeaux
Pessac 33607, France
Email: sojic@ubordeaux.fr

[d] P. C. Chaumet
Institute Fresnel, CNRS, Centrale Marseille
Aix Marseille University
Marseille 13013, France

[e] Prof. Dr. B. Su
General Surgery Department
Children's Hospital, Zhejiang University School of Medicine, National Clinical Research Center for Child Health
Hangzhou 310052, China

Supporting information for this article is given via a link at the end of the document.

Abstract: Deciphering and enhancing microbead-based electrochemiluminescence (ECL) immunoassays is imperative for sensitive disease-related biomarker detection. Herein we report the single-layer graphene-coated indium tin oxide (GITO) electrodes, with superior electrochemical activity, to accelerate the electrochemical oxidation of tri-*n*-propylamine by 9400-fold, thus enhancing the ECL generation from the $Ru(bpy)_3^{2+}$-labeled microbeads. Furthermore, the high transparency of the GITO electrode enables us to decipher the ECL generation by spatially mapping the distribution of ECL signals on single microbeads through ECL self-interference spectroscopy and inverted ECL microscopy. Additionally, the GITO electrode also allows the efficient collection of ECL signal from the electrode underneath. A comparative microscopic imaging of single microbeads in both upright and inverted configurations suggests that the inverted signal-collection mode can significantly reduce the optical loss, because the optical signal does not need to travel across the microbeads and bulk solution anymore, therefore achieving a 6-fold signal enhancement. This enhancement can translate into an increase of signal-to-noise ratio by 240% in the bead-based ECL immunoassays. The study provides valuable insights into the ECL generation in the bead-based ECL systems and an innovative strategy to enhance the sensitivity of immunoassays through the synergistic integration of single-layer graphene electrodes with an inverted signal-collection mode.

Introduction

Electrochemiluminescence (ECL) is a light emission event induced by electrochemical reactions, possessing unique advantages including low background, high sensitivity and excellent spatiotemporal controllability.[1-4] It has

served as one of the most powerful transduction tools in the in-vitro diagnostics.[5-8] Among various ECL systems, the tris(2,2'-bipyridine)ruthenium(II) ($Ru(bpy)_3^{2+}$)/tri-*n*-propylamine (TPrA) coreactant system is well-established and thought of as the cornerstone of ECL immunoassays, because it has been successfully integrated with immunorecognition for detecting more than 100 disease-related biomarkers and screening new biochemical drugs.[9-13] Despite great success, the ECL immunoassay with a pg/mL sensitivity cannot meet the requirement of detecting low-abundance biomarkers (fg/mL). Continuously increasing the sensitivity of ECL immunoassays therefore is of great significance.

In the commercial microbead-based ECL immunoassay, the light signal originates from the $Ru(bpy)_3^{2+}$ captured on the surface of micrometer-sized magnetic beads through immune and/or biological recognition reactions. In this scheme, the direct electrochemical oxidation of $Ru(bpy)_3^{2+}$ is spatially prohibited,[14-16] and the ECL signal is generated primarily via the so-called low oxidation potential (LOP) pathway, where only TPrA undergoes the electrochemical oxidation at the electrode surface and the generated intermediates, $TPrA^{+\bullet}$ and $TPrA^{\bullet}$, subsequently react with the $Ru(bpy)_3^{2+}$ to form the excited state $Ru(bpy)_3^{2+*}$ that eventually emits the light.[17-19] Metal and carbon are widely used as the electrode materials in the ECL immunoassay, since the electrochemical oxidation of TPrA is kinetically fast on them.[20-22] For example, the commercialized Roche immunoanalyzer use platinum as the electrode material.[9] But the ECL signal of immunoassays can be only collected from the upside of microbeads/electrode, because of the opaqueness of metal and carbon-based electrodes. In other words, the ECL signal mainly generated on the bottom surface of microbeads must be measured from their upside. In this case, the ECL signal suffers from the light scattering by the microbeads and the attenuation due to the partial transparency of the microbeads. Highly transparent and conductive metal oxides (for instance indium tin oxide, ITO) electrodes have been widely deployed in the ECL studies, particularly in ECL imaging, however they are unfit for the ECL immunoassays because of the sluggish electrochemical oxidation kinetics of TPrA on them.[23,24] Although a number of strategies have been elaborated to modify the electrodes to accelerate the electrochemical oxidation of TPrA,[25,26] the potency remains limited. Developing electrodes with both superior electrochemical activities and high transparency is imperative.

On the other hand, unraveling the reaction mechanisms of ECL generation on the microbead surface is also crucial for enhancing the detection sensitivity. Spatially mapping the distribution of ECL intensity on the microbead surface has imparted an interesting approach of elucidating the reaction mechanisms.[27-30] For example, three-dimensional ECL imaging of single polystyrene microbeads labeled with $Ru(bpy)_3^{2+}$ was realized by using an orthogonal side-view microscopy.[31,32] The ECL signal was found to be generated predominantly on the bead surface within a ca. 2–3 μm distance from the electrode, due to the short half-lifetime of $TPrA^{+\bullet}$. The variations of the ECL-emitting distance and the corresponding light intensity profile in the normal direction of the electrode surface over the time were also revealed.[33] Furthermore, by imaging $Ru(bpy)_3^{2+}$-labeled microbeads with diameters ranging from 0.3 μm to 2.8 μm, a highly efficient ECL-generation route near the electrode surface (less than 1 μm) was discovered.[8] Based on the mechanistic understanding of bead-based immunoassays, a variety of novel strategies have been proposed to enhance the ECL generation on the microbead surface to increase the sensitivity, including the use of redox mediators[34,35] and conductive microbeads.[36,37] Another technique of interest is the ECL self-interference spectroscopy (ECLIS), which with a precise spatial resolution allows the measurement of the vertical distribution of ECL intensity in the vicinity of the electrode surface,[38] and so provides insightful information on the reaction mechanisms.[35,39] It certainly holds a great promise for exploring the spatial distribution of the ECL signal on the microbead surface, but heavily impeded by the relatively weak ECL signal generated in this system, due to the poor electrochemical activity of the electrodes available. To be noted that, in this technique, the electrode must have a high transmittance, as the ECL self-interference results from the superposition of the ECL beam emitted directly by the excited-state luminophores and that reflected from the electrode interfaces. At an electrode with only a low light transmittance, the amplitude of reflected ECL beam will be severely attenuated and so the interference between two ECL beams will become ambiguous. A highly transparent and electrochemically active electrode is greatly to be desired in ECLIS.

Single-layer graphene, a two-dimensional carbon material with excellent conductivity, superior mechanical strength, and transparency, has emerged as a revolutionary material for diverse applications.[40-42] Its ability to facilitate the electrochemical oxidation of aliphatic amines also makes it ideal as the substrate electrode for ECL sensing and imaging.[43-45] Moreover, its high transmittance renders also a high ECL collection efficiency. However, in previously reported studies, the use of graphene for mechanistic exploration of ECL processes remains scarce. Here, we integrate single-layer graphene with ECL self-interference spectroscopy and microscopy techniques to investigate and rationalize ECL behavior in bead-based ECL immunoassays.

In this work, we report the preparation of a single-layer graphene-coated ITO electrode, designated as GITO, which exhibits outstanding electrochemical properties and a high transparency, comparable to those of glassy carbon (GC) and ITO electrodes, respectively. First, in comparison with an ITO electrode, the electrochemical oxidation of TPrA at the GITO is significantly accelerated, with an enhancement of approximately 9400-fold. As a result, the ECL intensity of $Ru(bpy)_3^{2+}$ freely diffusing in solution and labeled on the microbead surface is enhanced by 42-fold and 34-fold, respectively. Second, the use of GITO also allows the acquisition of ECL self-interference spectra of $Ru(bpy)_3^{2+}$-labeled microbeads that is infeasible when using other electrode materials. Thus, the spatial distribution of ECL signal on the microbead can be extracted from the ECL self-interference spectrum (as shown in **Scheme 1**, top panel). Moreover, the GITO also allows us to collect the ECL signal and map its spatial distribution on the microbead surface from the electrode underneath (bottom panel, **Scheme 1**). In addition, microscopic imaging of single microbeads in both upright and inverted configurations reveals that collecting the ECL signal from the electrode underneath can markedly reduce the optical loss, as the light signal does not need to travel through the microbeads and the bulk solution anymore, therefore achieving a 6-fold signal enhancement. As a proof-of-concept, bead-based immunoassay was finally performed using GITO as the electrode for the detection of human carcinoembryonic antigen (CEA). Indeed, the signal-to-noise ratio was enhanced by 240% if collecting the ECL signal from the electrode/microbeads underneath, in comparison with the conventional mode of acquiring the signal from the upside.

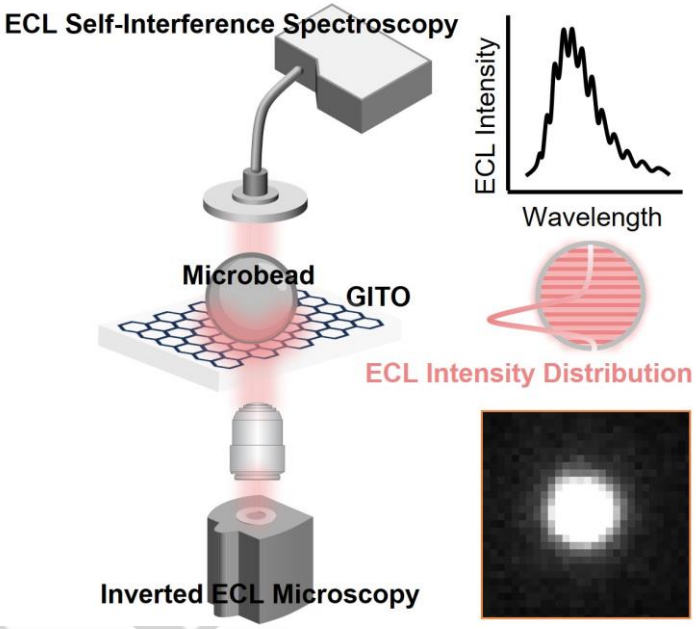

Scheme 1. Schematic of deciphering the ECL generation from a single microbead based on the GITO electrode by ECL self-interference spectroscopy (top) and inverted ECL microscopy (bottom).

Results and Discussion

As shown in **Figure 1a**, a single-layer graphene can be transferred onto the surface of ITO electrodes or other substrates via a wet stripping and transfer method. After coating with graphene, the surface of ITO turns hydrophobic with the water contact angle increased from 41.7° to 91.3° (**Figures 1b** and **1c**). The thickness and roughness of single-layer graphene are 1.55 nm and 1.29 nm, respectively, as determined by atomic force microscope (**Figure 1d**). Due to the ultrathin nature of monolayer graphene, the surface morphology of the GITO electrode remains largely unchanged after graphene transfer (**Figure S1**). Moreover, X-ray photoelectron and Raman spectra also confirm the graphene layer is indeed a monolayer with minimal defects (**Figure S2**). Importantly, as compared in **Figure 1e**, the single-layer graphene has a negligible effect on the transmittance of ITO. Both ITO and GITO exhibit a high transmittance of ca. 90%.

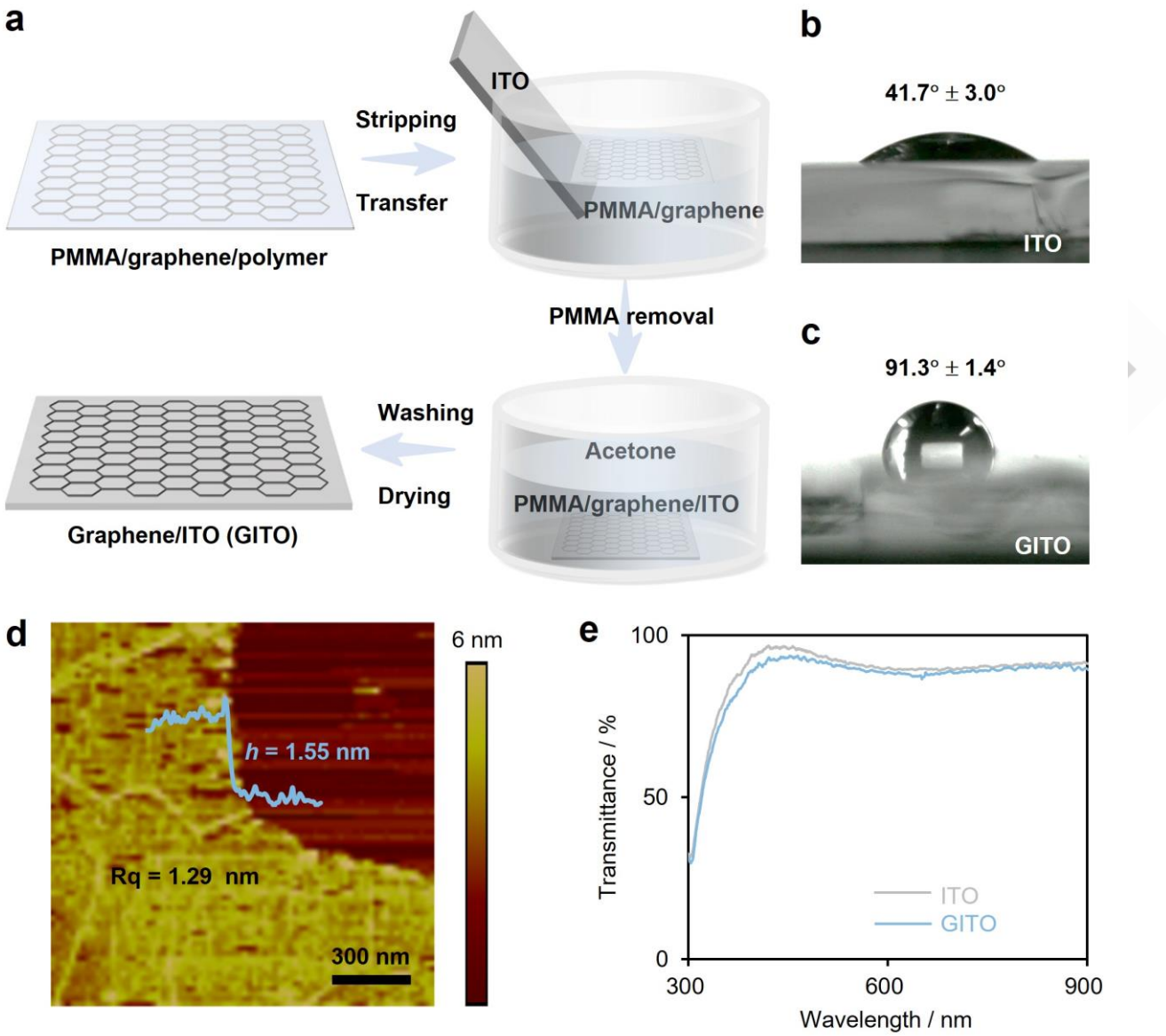

Figure 1. (a) Schematic fabrication of single-layer graphene on planar substrates by the stripping and transfer method. (b, c) Water contact angles of ITO (b) and GITO (c) surfaces. (d) Atomic force microscope (AFM) image of single-layer graphene. (e) UV-visible transmission spectra of ITO and GITO.

The electrochemical property of GITO was also studied. First, the electrochemical oxidation of $Ru(bpy)_3^{2+}$ at both ITO and GITO is kinetically fast, and therefore similar cyclic voltammograms (CVs) are observed (**Figure S3**). While as can be seen from linear scan voltammograms in **Figure 2a**, the electrochemical oxidation of TPrA at the GITO yields a mass-transport controlled current peak, akin to that at a glassy carbon (GC) electrode but noticeably different from the featureless and charge-transfer limited current at the ITO. This peak current is thousand-fold larger than that at an ITO at the same oxidation potentials. To quantitatively compare the performance of three electrodes toward the electrochemical oxidation of TPrA, the standard rate constant (k^0) was further derived according to the Butler–Volmer equation (**Figures S4** and **S5**). As compared in **Figure 2b**, k^0 at the GITO (0.94 $cm \cdot s^{-1}$) is indeed comparable to that at the GC (3.1 $cm \cdot s^{-1}$), but remarkably larger than that at the ITO (1.0×10^{-4} $cm \cdot s^{-1}$). Then, the ECL intensity of $Ru(bpy)_3^{2+}$/TPrA at the GITO was compared with that at the ITO and GC electrodes in the solution containing both 1 μM $Ru(bpy)_3^{2+}$ and 100 mM TPrA. In this condition, the ECL is predominantly generated via the LOP pathway. The ECL intensity at the GITO is a bit (3.6-fold) lower than that at the GC, but much higher than that at the ITO by 42-fold (**Figures 2c** and **2d**).

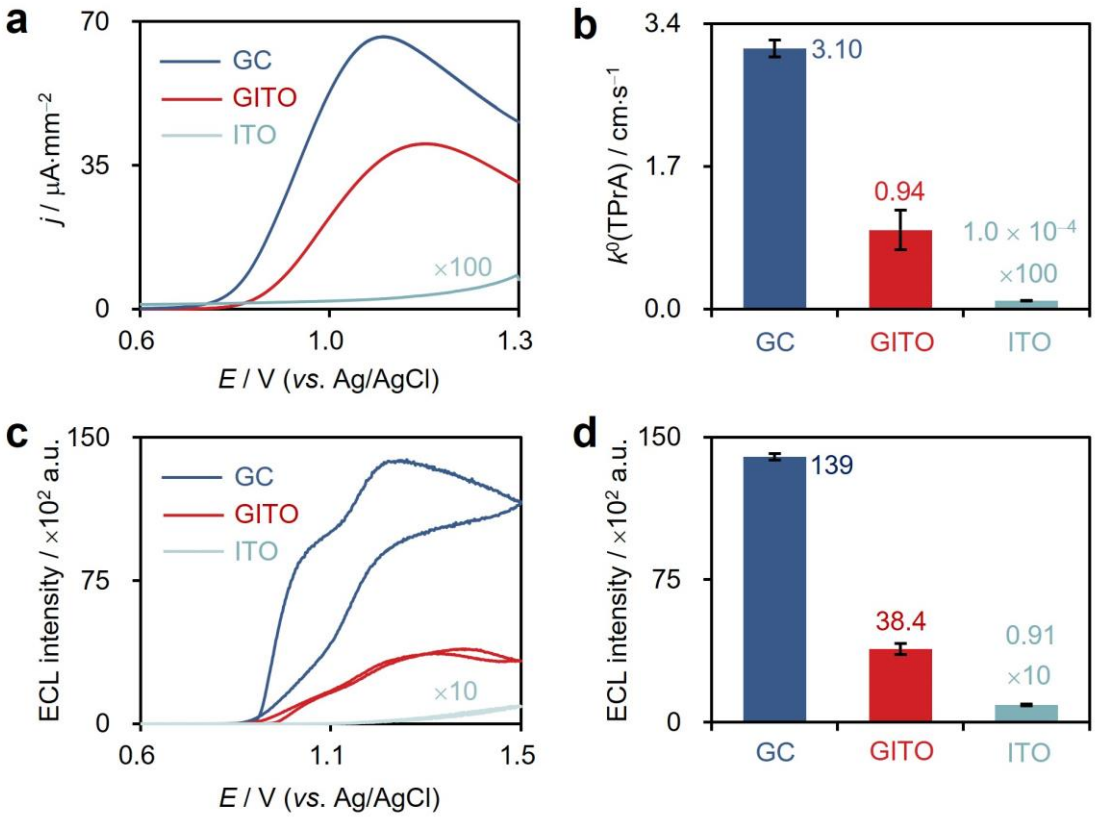

Figure 2. (a) Linear sweep voltammograms obtained at the GC, GITO and ITO electrodes in phosphate buffer (PB) solution (0.2 M, pH 7.4) with 100 mM TPrA. (b) k^0 of TPrA electrochemical oxidation on the three electrodes. The magnitudes of j and k^0 obtained at the ITO are multiplied by 100 for comparison. (c, d) ECL intensity-potential curves (c) and maximum intensities (d) measured at the three electrodes in 0.2 M PB solution (pH 7.4) containing both 1 μM $Ru(bpy)_3^{2+}$ and 100 mM TPrA. The ECL intensity at the ITO is 10-fold magnified for comparison.

Above results imply the great potential of GITO in mapping the distribution of ECL signal on the microbead surface. This information will be of great significance for optimizing the immunoassay sensitivity. However, spatial mapping of the ECL signal distribution on the microbead surface is so far exclusively based on the ECL imaging.[27-29] Although ECLIS has been well deployed to map the distribution of ECL signal generated by freely diffusing $Ru(bpy)_3^{2+}$ in solution,[35,39] it remains very difficult to record a well-defined ECL self-interference spectrum for the $Ru(bpy)_3^{2+}$ immobilized on microbeads using previously developed ITO or Au electrode. Indeed, these electrodes can only provide a weak ECL signal (limited by the slow electrochemical oxidation kinetics of TPrA) and a deficient transmittance (for Au electrode). Given the GITO possesses both superior electrochemical activities and a high transmittance, it can principally serve as an ideal electrode for ECLIS measurements. Therefore, using the above-mentioned method, single-layer graphene coated ITO/silica/silicon (GITO/SiO_2/Si) electrode was prepared by transferring the single-layer graphene onto the custom ITO/SiO_2/Si electrode, which consists of 102-nm-thick ITO and 6.05-μm-thick SiO_2 deposited on the silicon substrate (**Figure S6**). As proved by the white-light interferometry, the optical interferometric peaks in the wavelength range of 600 ~ 800 nm are nearly unchanged before and after the graphene transfer (**Figures 3a** and **3b**). Furthermore, the interferometric amplitude (namely the deviation between the interferometric spectrum and its envelope) of the GITO/SiO_2/Si is very close to that of the ITO/SiO_2/Si, but much larger than that of the Au/SiO_2/Si (**Figure S7**). So, it follows that the single-layer graphene does not affect the light interference thanks to its high transparency and that the GITO/SiO_2/Si is indeed more suitable as the substrate electrode for ECLIS.

$Ru(bpy)_3^{2+}$-labeled polystyrene microbeads (Ru-PSBs) that can mimic immunobeads were prepared by subjecting amino-functionalized PSBs with a diameter of 3.8 μm to an amide reaction with bis(2,2'-bipyridyl)(4-carboxypropyl-2,2'-bipyridyl)ruthenium(II). The successful attachment of $Ru(bpy)_3^{2+}$ to the surface of PSBs was confirmed by their bright photoluminescence (**Figure S8**). Subsequently, a single-layer of Ru-PSBs was prepared by drop-casting the suspension containing Ru-PSBs on the electrode surface to measure the ECL self-interference spectra (**Figure S9**). As shown in **Figure 3c**, the ECL self-interference results from the superposition of two ECL beams, one of which is emitted directly from the surface of Ru-PSBs. The other travels across the layer of Ru-PSBs and is then

reflected at the interfaces of GITO/SiO_2/Si electrode. It should be noted that only ill-defined ECL self-interference spectra were acquired for Ru-PSBs, if using ITO/SiO_2/Si and Au/SiO_2/Si electrodes (**Figure S10**). In contrast, the ECL self-interference spectrum was successfully obtained using the GITO/SiO_2/Si electrode (**Figure 3d**), though the amplitude of ECL self-interference spectrum of Ru-PSBs is much smaller than that of freely diffusing $Ru(bpy)_3^{2+}$ (**Figure S11**). This decrease can be largely ascribed to the relatively low transmittance of PSBs (**Figure S12**), causing a substantial attenuation of reflected ECL beam and thereby reducing the interference of two ECL beams.

To rationalize the generation of ECL self-interference for Ru-PSBs and to calculate the thickness/position of ECL-emitting layer, a microbead-based self-interference model was established (see **Section S3.7**, **Figures S13** and **S14** in supporting information for details). Briefly, the ECL signal generated on the surface of Ru-PSBs was divided into a number of sublayers along the normal direction of the electrode surface (**Figure 3e**). The ECL self-interference spectrum of each sublayer was calculated by the MATLAB software, and the superposition of all the sublayer spectra yielded a theoretical ECL self-interference spectrum. When this theoretical spectrum best matching with that recorded experimentally (**Figure 3f**), the position/height of the highest sublayer is defined as the thickness of the ECL-emitting layer. In this way, the thickness of ECL-emitting layer on Ru-PSBs obtained by ECLIS is 770 ± 60 nm.

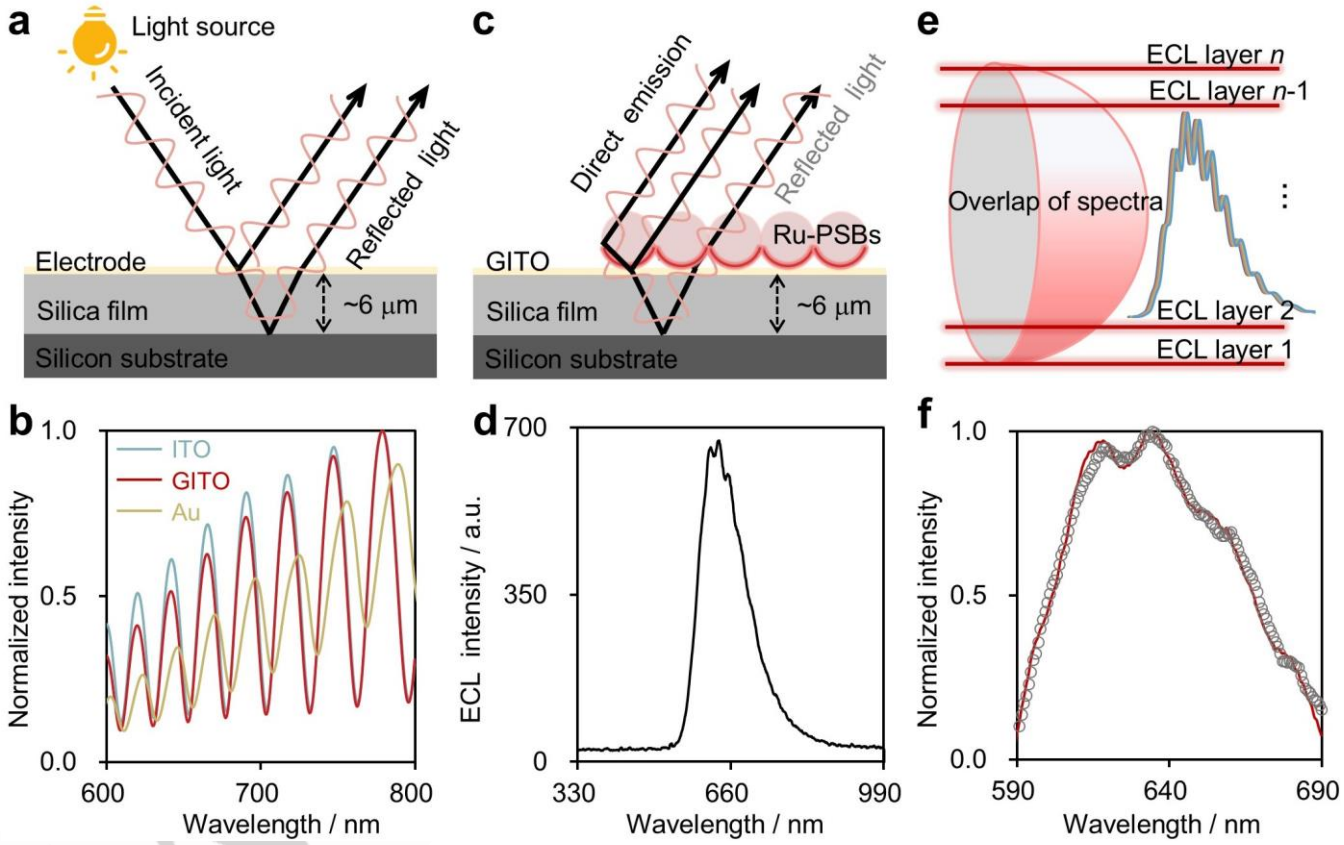

Figure 3. (a) Schematic principle of the white light interferometry. (b) Normalized white light interferometric spectra at the ITO/SiO_2/Si (blue), GITO/SiO_2/Si (red) and Au/SiO_2/Si (yellow) electrodes. (c) Schematic of the ECL self-interference of Ru-PSBs. (d) ECL self-interference spectrum of single-layer Ru-PSBs on the GITO/SiO_2/Si electrode obtained in 0.2 M PB solution (pH 7.4) containing 100 mM TPrA. The applied potential was +1.5 V (*vs.* Ag/AgCl) and the spectral integration time was 2 s. (e) Schematic of calculating the thickness of the ECL-emitting layer on a single Ru-PSB. (f) Normalized experimental (solid red line) and theoretical (open circles) ECL self-interference spectra of Ru-PSBs.

Subsequently, ECL imaging was employed to further investigate the ECL distribution on the surface of individual Ru-PSBs. First, ECL generation by individual Ru-PSBs on the ITO, GITO, and GC electrodes was comparatively studied by imaging single Ru-PSBs using an upright microscope (upright configuration, **Scheme 2**). As shown in **Figures 4a** and **S15**, compared with an ITO, the ECL intensity of single Ru-PSBs on the GITO is enhanced by 34-fold, although it is still 2-3 times lower than that on the GC electrode. The lower ECL intensity compared to the GC electrode can be attributed to residual polymeric contaminants (e.g., PMMA), which partially obstruct electroactive sites on the GITO surface and thus impede the electron transfer. Moreover, thanks to the high transparency of the GITO, the ECL images of single Ru-PSBs can be also recorded from the underneath of GITO by using an inverted

microscope (inverted configuration, **Scheme 2**). It is very interesting to see that the ECL intensity of single Ru-PSBs is enhanced by 6-fold in comparison with that in the upright mode (**Figure 4b**). Apart from the difference in optics, such as optical path and objective lens used, between these two imaging configurations, this enhancement can be connected with the significant reduction of the light loss arising from the light scattering and attenuation by partially opaque PSBs and in solution. On the other hand, the ECL area of Ru-PSBs is also decreased by 52% when switching from the upright to the inverted configuration (**Figures 4b-f** and **S16**). This decrease can be ascribed to the dramatic decline of ECL intensity on the microbead surface with increasing the distance from the electrode surface, since most of ECL photons are emitted from the bottom surface of the microbead via the so-called LOP route. In this case, in the upright configuration where the objective lens is placed on the upside of Ru-PSBs, most of ECL photons must travel across the microbead and solution, leading to the overestimation of ECL area due to the multiple refractions and scattering of ECL at the microbead-solution interface (**Figure S17**). In contrast, in the inverted imaging configuration where the objective is placed beneath the Ru-PSBs, the ECL photons can be directly and efficiently collected (**Figure S17**).The results suggest that collecting the ECL signal from the underneath of Ru-PSBs can not only minimize the loss of optical signal due to partially opaque microbeads and in solution, but also reduce the error in determining the ECL area of single Ru-PSBs by obviating the effects of scattering, reflection and refraction.

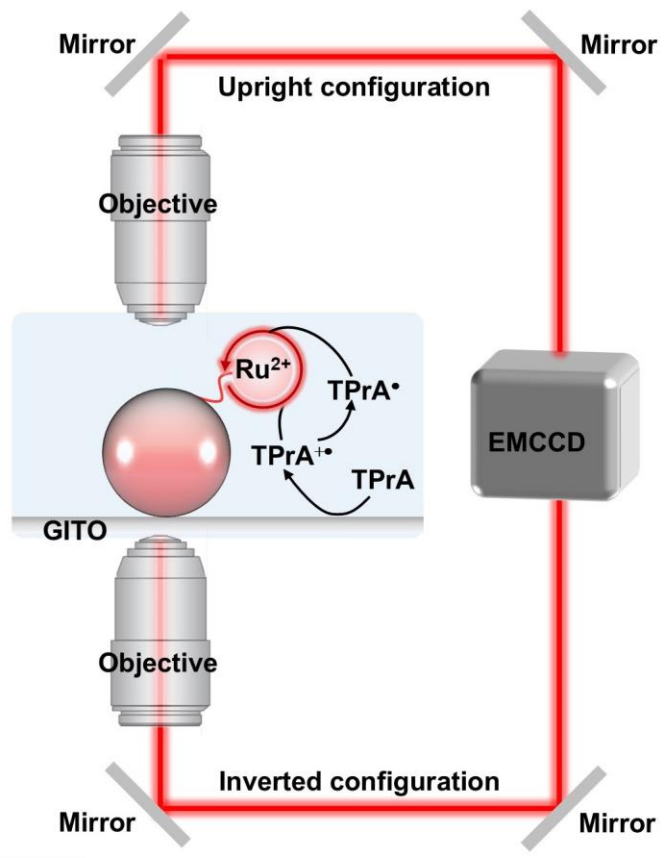

Scheme 2. Schematic of ECL microscope for capturing the ECL images of single Ru-PSBs under the upright (top) and inverted (bottom) imaging configurations.

To rationalize the variations of ECL intensity and ECL area of single Ru-PSBs in two imaging configurations, finite element simulations were performed. First, the distribution of ECL intensity on a single Ru-PSB surface was calculated using the COMSOL Multiphysics software (see **Section S5**, **Figure S18** and **Tables S1-S5** in supporting information for details). Since it is difficult to take into account the optical effects of microbead and electrode in the finite element simulations, there is a discrepancy between calculated and experimentally captured ECL images (**Figure S19**). So, optical simulations (see details in **Section S6** in supporting information file) based on the discrete dipole approximation were further conducted to reconstruct the spatial distribution of the ECL intensity on the microbead surface.[46-49] In the optical simulations, the parameters of the lens, including the magnification and numerical aperture, were considered for the two configurations, excluding the error due to the light collection efficiency of lens and allowing a reliable evaluation of the impact of acquisition mode on the ECL intensity of Ru-

PSBs. As shown in **Figures 4g** and **4h**, the calculated ECL image of a Ru-PSB in the inverted configuration shows a much brighter light emitting spot than that in the upright configuration, consistent with the experimental results, confirming that the detection in the inverted configuration can indeed increase the collection efficiency of ECL photons emitted by Ru-PSBs. However, the simulation results also identify a decrease of ECL intensity at the radial center of the microbead, being different than the experimental images (**Figure S20**). The difference is most likely associated with the omission of multiple light reflections and refractions at the microbead-solution interface in the simulations. Nevertheless, the ECL images obtained in the inverted configuration can more accurately reflect the distribution of ECL intensity on the microbead surface. As displayed in **Figure S21**, the thickness of ECL-emitting layer on Ru-PSBs is estimated to be 1130 ± 140 nm according to the ECL area in the inverted image, which is a bit larger than that obtained from ECLIS. The discrepancy is likely connected with a relatively low photon collection efficiency of the fiber optic spectrometer compared with the electron multiplying charge coupled device (EMCCD) camera, so limiting its ability to register weak light emitted at a large distance from the electrode surface. Therefore, a combination of ECLIS and ECL imaging enables an accurate analysis of the ECL generation by Ru-PSBs, offering valuable insights into the reaction mechanisms for improving the performance of microbead-based ECL immunoassays.

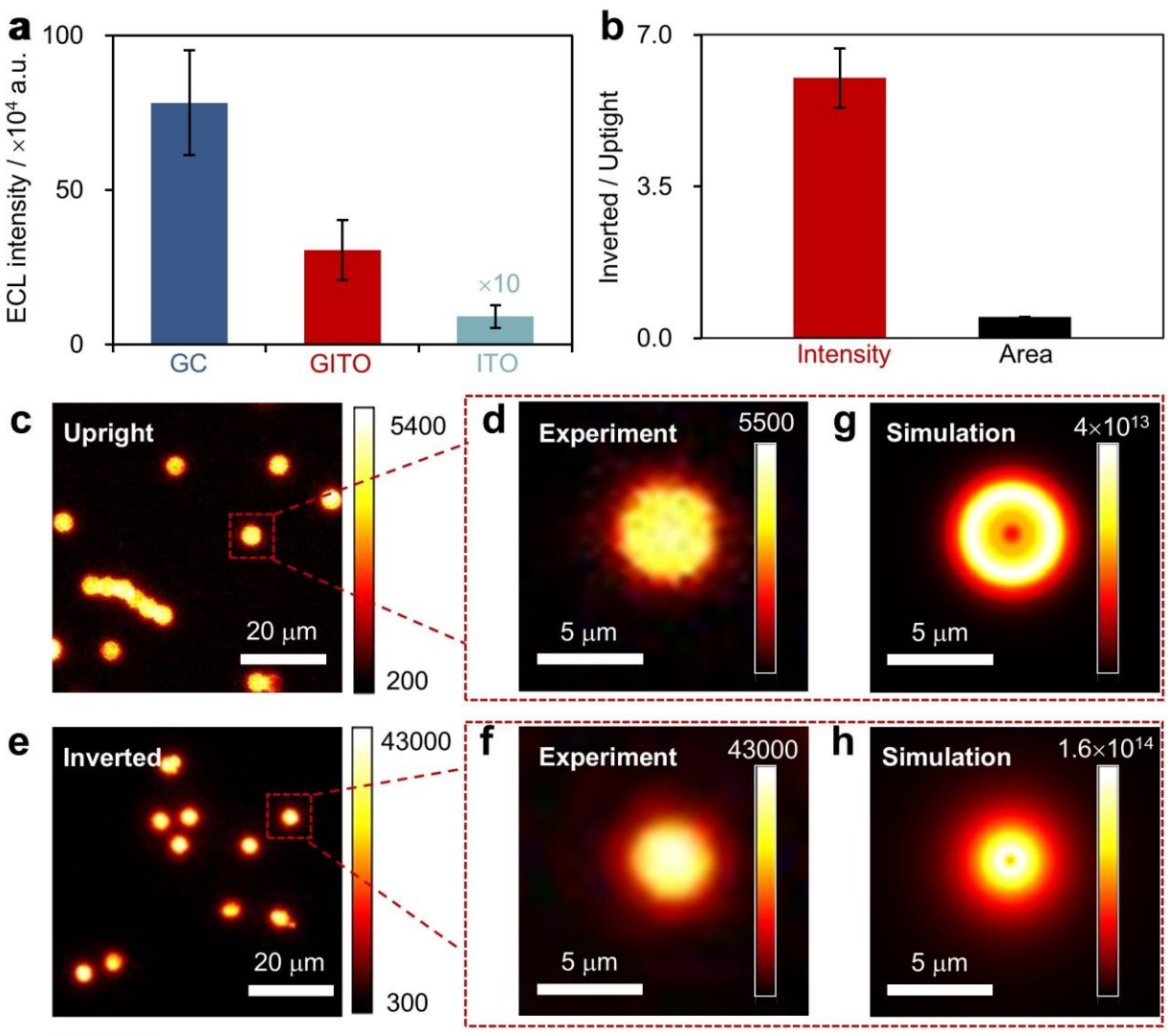

Figure 4. (a) The ECL intensity of single Ru-PSBs on different electrodes using the upright configuration. (b) The relative ECL intensity and ECL area of single Ru-PSBs obtained using the upright and inverted configurations. The data represents the statistical counting of 100 single beads. (c-f) ECL images of Ru-PSBs experimentally captured in the upright (c, d) and inverted (e, f) configurations. (g, h) Simulated ECL images of a single bead in the upright (g) and inverted (h) configurations.

As demonstrated above, collecting the ECL signal from the bottom of electrode/microbeads can enhance the collected intensity of signal and potentially increase the sensitivity of microbead-based immunoassay. So, an ECL immunoassay was comparatively conducted for the detection of CEA, as shown in **Figure 5a**, under two signal

collection configurations, namely the bottom generation-bottom collection (BG-BC) and bottom generation-top collection (BG-TC) modes. First, CEA, $Ru(bpy)_3^{2+}$-conjugated detection antibody and biotin-labeled capture antibody were incubated in a phosphate buffer saline (PBS) to form the immunocomplexes, which were then captured onto the streptavidin-labeled magnetic microbeads. Subsequently, the beads were separated, washed and immobilized on the GITO electrode surface via a permanent magnet (**Figure S22a**). Finally, the ECL signal was collected under the BG-BC and BG-TC configurations, using a photomultiplier tube (PMT) as the detector (**Figures 5a** and **S22b**). As displayed in **Figure 5b**, the ECL signal collected in the BG-BC mode is indeed higher than that in the other mode, with an approximately 2.4-fold increase in the signal-to-noise ratio (S/N). The improved SNR is anticipated to significantly enhance the analytical sensitivity, facilitating the detection of low-abundance targets.[50-52]

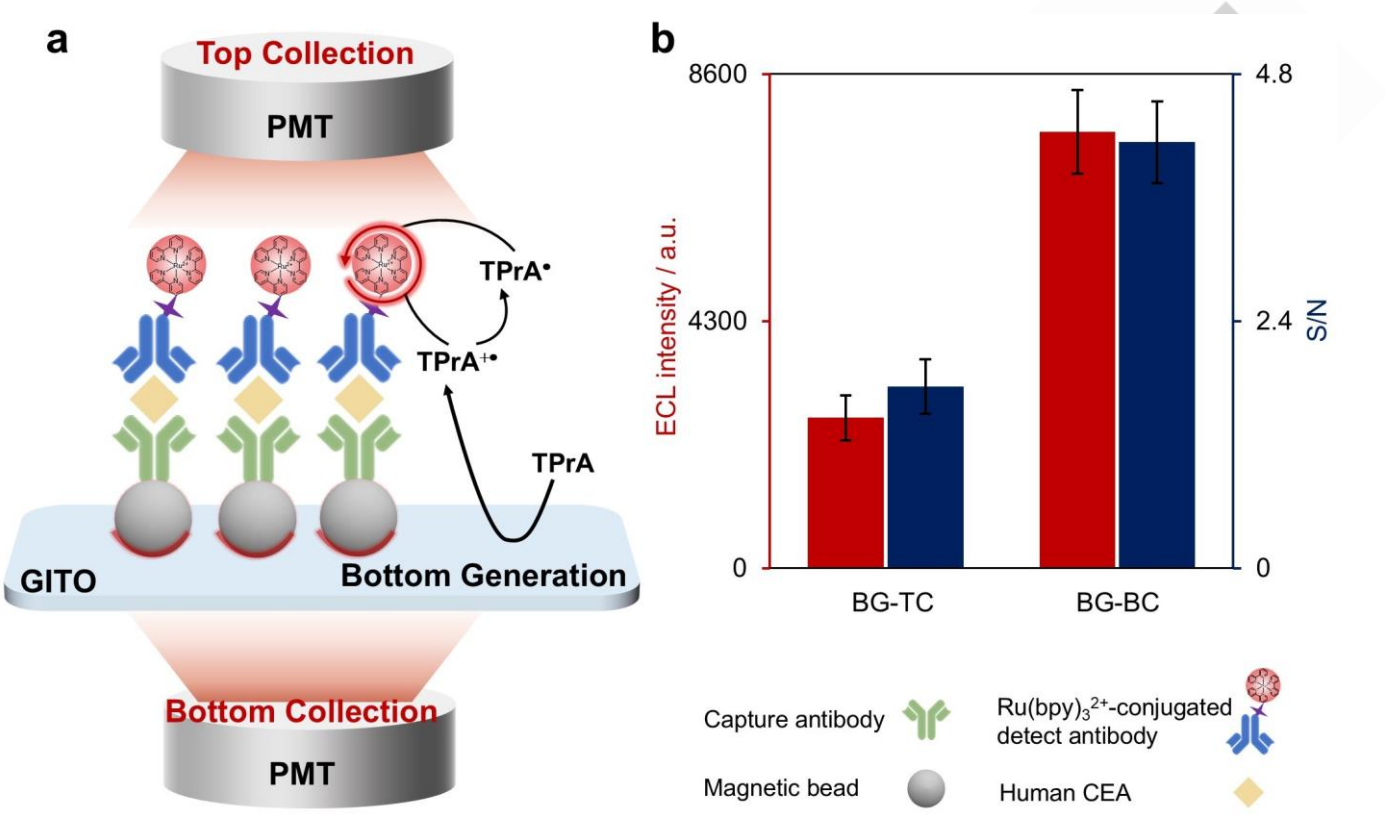

Figure 5. (a) Schematic of the BG-TC and BG-BC modes for microbead-based ECL immunoassays. (b) ECL intensity (red) and the signal-to-noise ratio (S/N, blue) of the immunoassay recorded in 0.2 M PB solution (pH 7.4) with 100 mM TPrA. The concentration of CEA was 25 ng·mL^{-1} and the applied potential was +1.5 V (*vs.* Ag/AgCl). Standard deviation, n = 3.

Conclusion

In summary, transparent single-layer graphene electrodes combining the outstanding electrochemical properties with the high optical transmittance were fabricated and used to unravel the ECL generation in the microbead system and enhance its performance. The superior electrochemical activity of GITO promotes the electrochemical oxidation of TPrA by 9400-fold in comparison with the pristine ITO, leading to a 34-fold enhancement in the ECL intensity of Ru-PSBs. Moreover, the high transparency of GITO enables the spatially-resolved measurement of the distribution of ECL signal on Ru-PSBs, with an ECL-emitting layer thickness determined to be 770 ± 60 nm and 1130 ± 140 nm by ECLIS and inverted ECL imaging, respectively. In addition, as proved by ECL imaging of single Ru-PSBs in the upright and inverted configurations, the ECL signal can be enhanced by up to 6-fold when collecting the signal from the electrode/microbead underneath rather than from the upside, because the optical loss caused by propagation of light through the microbeads and solution is remarkably decreased. Finally, based on this strategy, the signal-to-noise ratio of microbead-based ECL immunoassay can be enhanced by 240%. The results demonstrate the versatility of single-layer graphene electrodes and their merits for applications in ECL spectroscopy, microscopic imaging and ultrasensitive ECL bioassays. We are using the transparent single-layer graphene electrode, in conjunction with nanostructured luminophores, to detect low-abundance biomarkers, and the results will be reported soon later elsewhere.

Acknowledgements

This work is financially supported by the National Natural Science Foundation of China (22125405, 22204142) and the ANR (MAPICS-ANR-23-CE42-0018-02). The authors would like to thank Mrs. Fang Chen (Chemistry Instrumentation Center of the Chemistry Department) for technical assistance with SEM measurements, Mrs. Chen Chen (Chemistry Instrumentation Center of the Chemistry Department) for her help on Raman measurement and analysis, and Dr. Yangfan Lu (School of Materials Science and Engineering) for her help on XPS measurement and analysis.

Keywords: electrochemiluminescence • single-layer graphene • microbead-based immunoassays • inverted imaging • self-interference spectroscopy

[1] M. Hesari, Z. Ding, Review—Electrogenerated Chemiluminescence: Light Years Ahead. *J. Electrochem. Soc.* **2015**, *163*, H3116.

[2] L. Hu, G. Xu, Applications and Trends in Electrochemiluminescence. *Chem. Soc. Rev.* **2010**, *39*, 3275.

[3] G. Valenti, E. Rampazzo, S. Kesarkar, D. Genovese, A. Fiorani, A. Zanut, F. Palomba, M. Marcaccio, F. Paolucci, L. Prodi, Electrogenerated Chemiluminescence from Metal Complexes-Based Nanoparticles for Highly Sensitive Sensors Applications. *Coord. Chem. Rev.* **2018**, *367*, 65.

[4] Z. Liu, W. Qi, G. Xu, Recent Advances in Electrochemiluminescence. *Chem. Soc. Rev.* **2015**, *44*, 3117.

[5] F. Du, Y. Chen, C. Meng, B. Lou, W. Zhang, G. Xu, Recent Advances in Electrochemiluminescence Immunoassay Based on Multiple-Signal Strategy. *Curr. Opin. Electrochem.* **2021**, *28*, 100725.

[6] L. Yang, J. Li, Recent Advances in Electrochemiluminescence Emitters for Biosensing and Imaging of Protein Biomarkers. *Chemosensors* **2023**, *11*, 432.

[7] A. Chen, W. Liang, H. Wang, Y. Zhuo, Y. Chai, R. Yuan, Anodic Electrochemiluminescence of Carbon Dots Promoted by Nitrogen Doping and Application to Rapid Cancer Cell Detection. *Anal. Chem.* **2020**, *92*, 1379.

[8] A. Zanut, A. Fiorani, S. Canola, T. Saito, N. Ziebart, S. Rapino, S. Rebeccani, A. Barbon, T. Irie, H.-P. Josel, F. Negri, M. Marcaccio, M. Windfuhr, K. Imai, G. Valenti, F. Paolucci, Insights into the Mechanism of Coreactant Electrochemiluminescence Facilitating Enhanced Bioanalytical Performance. *Nat. Commun.* **2020**, *11*, 2668.

[9] N. Sojic, in *Analytical Electrogenerated Chemiluminescence: From Fundamentals to Bioassays, Vol. 15* (Ed.: N. Sojic), The Royal Society of Chemistry, **2020**, pp. 433-469.

[10] F. Deiss, C. N. LaFratta, M. Symer, T. M. Blicharz, N. Sojic, D. R. Walt, Multiplexed Sandwich Immunoassays Using Electrochemiluminescence Imaging Resolved at the Single Bead Level. *J. Am. Chem. Soc.* **2009**, *131*, 6088.

[11] W. Guo, H. Ding, C. Gu, Y. Liu, X. Jiang, B. Su, Y. Shao, Potential-Resolved Multicolor Electrochemiluminescence for Multiplex Immunoassay in a Single Sample. *J. Am. Chem. Soc.* **2018**, *140*, 15904.

[12] M. Sornambigai, L. Bouffier, N. Sojic, S. S. Kumar, Tris(2,2'-bipyridyl)ruthenium (II) Complex as a Universal Reagent for the Fabrication of Heterogeneous Electrochemiluminescence Platforms and Its Recent Analytical Applications. *Anal. Bioanal. Chem.* **2023**, *415*, 5875.

[13] A. Barhoum, Z. Altintas, K. S. S. Devi, R. J. Forster, Electrochemiluminescence Biosensors for Detection of Cancer Biomarkers in Biofluids: Principles, Opportunities, and Challenges. *Nano Today* **2023**, *50*, 101874.

[14] L. S. Dolci, S. Zanarini, L. D. Ciana, F. Paolucci, A. Roda, Development of a New Device for Ultrasensitive Electrochemiluminescence Microscopy Imaging. *Anal. Chem.* **2009**, *81*, 6234.

[15] W. Zhu, J. Dong, G. Ruan, Y. Zhou, J. Feng, Quantitative Single-Molecule Electrochemiluminescence Bioassay. *Angew. Chem. Int. Ed.* **2023**, *62*, e202214419.

[16] W. Fu, X. Wang, X. Ying, T. Sun, Y. Wang, J. Wang, B. Su, Electrochemiluminescence Lateral Flow Immunoassay Using Ruthenium(II) Complex-Loaded Dendritic Mesoporous Silica Nanospheres for Highly Sensitive and Quantitative Detection of SARS-CoV-2 Nucleocapsid Protein. *Adv. Funct. Mater.* **2024**, *34*, 2409632.

[17] W. J. Miao, J. P. Choi, A. J. Bard, Electrogenerated Chemiluminescence 69: The Tris(2,2'-bipyridine)ruthenium(II), $(Ru(Bpy)_3^{2+})$/Tri-*n*-propylamine (TPrA) System Revisited-a New Route Involving $TPrA^{\bullet+}$ Cation Radicals. *J. Am. Chem. Soc.* **2002**, *124*, 14478.

[18] X. Huang, B. Li, Y. Lu, Y. Liu, S. Wang, N. Sojic, D. Jiang, B. Liu, Direct Visualization of Nanoconfinement Effect on Nanoreactor via Electrochemiluminescence Microscopy. *Angew. Chem. Int. Ed.* **2023**, *62*, e202215078.

[19] A. Zanut, F. Palomba, M. Rossi Scota, S. Rebeccani, M. Marcaccio, D. Genovese, E. Rampazzo, G. Valenti, F. Paolucci, L. Prodi, Dye-Doped Silica Nanoparticles for Enhanced ECL-Based Immunoassay Analytical Performance. *Angew. Chem. Int. Ed.* **2020**, *59*, 21858.

[20] G. Valenti, A. Fiorani, H. Li, N. Sojic, F. Paolucci, Essential Role of Electrode Materials in Electrochemiluminescence Applications. *ChemElectroChem* **2016**, *3*, 1990.

[21] X.-H. Xu, A. J. Bard, Electrogenerated Chemiluminescence. 55. Emission from Adsorbed $Ru(bpy)_3^{2+}$ on Graphite, Platinum, and Gold. *Langmuir* **1994**, *10*, 2409.

[22] S. Parveen, Y. Chen, Y. Yuan, L. Hu, W. Zhang, M. R. H. S. Gilani, Y. Shi, R. Aziz ur, G. Xu, Electrochemiluminescence of $[Ru(bpy)_3]^{2+}$/Tripropylamine at Glassy Carbon, Platinum, and Palladium Electrodes. *Sens. Actuators Rep.* **2021**, *3*, 100062.

[23] T. Li, J. Ding, Y. Wang, B. Su, Regulating the Work Function and Surface Hydrophobicity of an Indium Tin Oxide Electrode for Enhanced Electrochemiluminescence Analysis. *Chem. Commun.* **2024**, *60*, 15007.

[24] J. Ding, P. Zhou, B. Su, Quantum Efficiency of Electrochemiluminescence Generation by Tris(2,2'-bipyridine)ruthenium(II) and Tri-*n*-propylamine Revisited from a Kinetic Reaction Model. *ChemElectroChem* **2022**, *9*, e202200236.

[25] R. Huang, M.-Y. Wei, L.-H. Guo, Enhanced Electrogenerated Chemiluminescence of $Ru(Bpy)_3^{2+}$/Tripropylamine System on Indium Tin Oxide Nanoparticle Modified Transparent Electrode. *J. Electroanal. Chem.* **2011**, *656*, 136.

[26] F.-R. F. Fan, A. J. Bard, Observing Single Nanoparticle Collisions by Electrogenerated Chemiluminescence Amplification. *Nano Lett.* **2008**, *8*, 1746.

[27] P. Dutta, D. Han, B. Goudeau, D. Jiang, D. Fang, N. Sojic, Reactivity Mapping of Luminescence in Space: Insights into Heterogeneous Electrochemiluminescence Bioassays. *Biosens. Bioelectron.* **2020**, *165*, 112372.

[28] Y. Feng, W. Zhou, X. Wang, J. Zhang, M. Zou, C. Zhang, H. Qi, Imaging and Simulation of Ruthenium Derivative Coating Microbeads at the Opaque Electrode with Electrogenerated Chemiluminescence. *Chem. Biomed. Imaging* **2023**, *1*, 648.

[29] Y. Wang, B. Su, Deciphering the Mechanisms of Electrochemiluminescence by Spatially Resolved Measurements. *Anal. Sens.* **2021**, *1*, 148.

[30] Y. Feng, C. Wang, W. Zhou, X. Yang, F. Paolucci, G. Valenti, H. Qi, Tomography Electrogenerated Chemiluminescence Imaging from Magnetic Microbeads. *Small* **2025**, *21*, 2500804.

[31] M. Sentic, M. Milutinovic, F. Kanoufi, D. Manojlovic, S. Arbault, N. Sojic, Mapping Electrogenerated Chemiluminescence Reactivity in Space: Mechanistic Insight into Model Systems Used in Immunoassays. *Chem. Sci.* **2014**, *5*, 2568.

[32] A. Fiorani, D. Han, D. Jiang, D. Fang, F. Paolucci, N. Sojic, G. Valenti, Spatially Resolved Electrochemiluminescence through a Chemical Lens. *Chem. Sci.* **2020**, *11*, 10496.

[33] D. Han, D. Fang, G. Valenti, F. Paolucci, F. Kanoufi, D. Jiang, N. Sojic, Dynamic Mapping of Electrochemiluminescence Reactivity in Space: Application to Bead-Based Assays. *Anal. Chem.* **2023**, *95*, 15700.

[34] A. Fracassa, C. I. Santo, E. Kerr, S. Knežević, D. J. Hayne, P. S. Francis, F. Kanoufi, N. Sojic, F. Paolucci, G. Valenti, Redox-Mediated Electrochemiluminescence Enhancement for Bead-Based Immunoassay. *Chem. Sci.* **2024**, *15*, 1150.

[35] N. S. Adamson, S. J. Blom, E. H. Doeven, T. U. Connell, C. Hadden, S. Knežević, N. Sojic, A. Fracassa, G. Valenti, F. Paolucci, J. Ding, Y. Wang, B. Su, C. Hua, P. S. Francis, Electrochemiluminescence Enhanced by a Non-Emissive Dual Redox Mediator. *Angew. Chem. Int. Ed.* **2024**, *63*, e202412097.

[36] X. Yang, J. Hang, W. Qu, Y. Wang, L. Wang, P. Zhou, H. Ding, B. Su, J. Lei, W. Guo, Z. Dai, Gold Microbeads Enabled Proximity Electrochemiluminescence for Highly Sensitive and Size-Encoded Multiplex Immunoassays. *J. Am. Chem. Soc.* **2023**, *145*, 16026.

[37] S. Rebeccani, C. Wetzl, V. A. Zamolo, A. Criado, G. Valenti, F. Paolucci, M. Prato, Electrochemiluminescent Immunoassay Enhancement Driven by Carbon Nanotubes. *Chem. Commun.* **2021**, *57*, 9672.

[38] Y. Wang, W. Guo, Q. Yang, B. Su, Electrochemiluminescence Self-Interference Spectroscopy with Vertical Nanoscale Resolution. *J. Am. Chem. Soc.* **2020**, *142*, 1222.

[39] Y. Wang, J. Ding, P. Zhou, J. Liu, Z. Qiao, K. Yu, J. Jiang, B. Su, Electrochemiluminescence Distance and Reactivity of Coreactants Determine the Sensitivity of Bead-Based Immunoassays. *Angew. Chem. Int. Ed.* **2023**, *62*, e202216525.

[40] W. Nan, J. Lin, L. Xu, L. Han, D. Zhan, Modulating the Interfacial Electrochemical Behavior of Single Layer Graphene. *Curr. Opin. Electrochem.* **2025**, *49*, 101608.

[41] K. S. Novoselov, A. K. Geim, S. V. Morozov, D. Jiang, Y. Zhang, S. V. Dubonos, I. V. Grigorieva, A. A. Firsov, Electric Field Effect in Atomically Thin Carbon Films. *Science* **2004**, *306*, 666.

[42] W. Li, M. Wojcik, K. Xu, Optical Microscopy Unveils Rapid, Reversible Electrochemical Oxidation and Reduction of Graphene. *Nano Lett.* **2019**, *19*, 983.

[43] T. Watanabe, R. Ishikawa, N. Hara, T. Iwasaki, M. Miyachi, Y. Shiigi, M. Takahashi, D. Kuroki, S. Koh, Single-Layer Graphene as a Transparent Electrode for Electrogenerated Chemiluminescence Biosensing. *Electrochem. Commun.* **2022**, *138*, 107290.

[44] E. K. Walker, D. A. Vanden Bout, K. J. Stevenson, Carbon Optically Transparent Electrodes for Electrogenerated Chemiluminescence. *Langmuir* **2012**, *28*, 1604.

[45] G. Valenti, M. Zangheri, S. E. Sansaloni, M. Mirasoli, A. Penicaud, A. Roda, F. Paolucci, Transparent Carbon Nanotube Network for Efficient Electrochemiluminescence Devices. *Chem. Eur. J* **2015**, *21*, 12640.

[46] D. Han, D. Jiang, G. Valenti, F. Paolucci, F. Kanoufi, P. C. Chaumet, D. Fang, N. Sojic, Optics Determines the Electrochemiluminescence Signal of Bead-Based Immunoassays. *ACS Sens.* **2023**, *8*, 4782.

[47] P. C. Chaumet, The Discrete Dipole Approximation: A Review. *Mathematics* **2022**, *10*, 3049.

[48] P. C. Chaumet, T. Zhang, A. Sentenac, Fast Far-Field Calculation in the Discrete Dipole Approximation. *J. Quant. Spectrosc. Radiat. Transf.* **2015**, *165*, 88.

[49] L. Oliveira, W. H. Campos, M. S. Rocha, Optical Trapping and Manipulation of Superparamagnetic Beads Using Annular-Shaped Beams. *Methods Protoc.* **2018**, *1*, 44.

[50] R. R. Williams, Fundamental Limitations on the Use and Comparison of Signal-to-Noise Ratios. *Anal. Chem.* **1991**, *63*, 1638.

[51] X. Liu, S. Zhao, Y. Xu, B. Zhang, J. Huang, F. Liu, N. Yang, W. Lu, D. Shi, D. Xie, Y. Hou, G. Wang, A Novel High-Throughput and Sensitive Electrochemiluminescence Immunoassay System. *Bioengineering* **2024**, *11*, 885.

[52] M. M. Sanagi, S. L. Ling, Z. Nasir, D. Hermawan, W. A. Wan Ibrahim, A. A. Naim, Comparison of Signal-to-Noise, Blank Determination, and Linear Regression Methods for the Estimation of Detection and Quantification Limits for Volatile Organic Compounds by Gas Chromatography. *J AOAC Int.* **2009**, *92*, 1833.

Entry for the Table of Contents

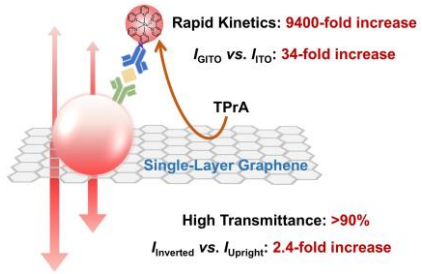

Single-layer graphene-coated indium tin oxide electrodes (GITO), with over 90% transparency and ultrafast electron transfer kinetics, enable a 9400-fold enhancement in the electrochemical oxidation of tri-*n*-propylamine and a 34-fold increase in electrochemiluminescence (ECL) from $Ru(bpy)_3^{2+}$-labeled microbeads compared to ITO. Moreover, inverted detection through GITO also boosts the signal-to-noise by 2.4-fold in ECL immunoassay by minimizing optical loss.

WILEY-VCH

RESEARCH ARTICLE

Transparent Single-Layer Graphene Electrodes for Deciphering and Enhancing Microbead-Based Electrochemiluminescence Immunoassay

Jialian Ding,[a] Yafeng Wang,[b] Leslie R. Arias-Aranda,[c] Patrick C. Chaumet,[d] Neso Sojic*[c] and Bin Su*[a, e]

[a] J. L. Ding, Prof. Dr. B. Su
State Key Laboratory of Soil Pollution Control and Safety, Zhejiang Key Laboratory of Excited-State Energy Conversion and Energy Storage, Department of Chemistry
Zhejiang University
Hangzhou 310058, China
E-mail: subin@zju.edu.cn

[b] Y. F. Wang
Department of Clinical Laboratory, Sir Run Run Shaw Hospital
Zhejiang University School of Medicine
Hangzhou 310016, China

[c] L. R. Arias-Aranda, Prof. N. Sojic
CNRS, Bordeaux INP, ISM, UMR 5255, ENSMAC
University of Bordeaux
Pessac 33607, France
Email: sojic@ubordeaux.fr

[d] P. C. Chaumet
Institute Fresnel, CNRS, Centrale Marseille
Aix Marseille University
Marseille 13013, France

[e] Prof. Dr. B. Su
General Surgery Department
Children's Hospital, Zhejiang University School of Medicine, National Clinical Research Center for Child Health
Hangzhou 310052, China

Supporting information for this article is given via a link at the end of the document.

Abstract: Deciphering and enhancing microbead-based electrochemiluminescence (ECL) immunoassays is imperative for sensitive disease-related biomarker detection. Herein we report the single-layer graphene-coated indium tin oxide (GITO) electrodes, with superior electrochemical activity, to accelerate the electrochemical oxidation of tri-*n*-propylamine by 9400-fold, thus enhancing the ECL generation from the $Ru(bpy)_3^{2+}$-labeled microbeads. Furthermore, the high transparency of the GITO electrode enables us to decipher the ECL generation by spatially mapping the distribution of ECL signals on single microbeads through ECL self-interference spectroscopy and inverted ECL microscopy. Additionally, the GITO electrode also allows the efficient collection of ECL signal from the electrode underneath. A comparative microscopic imaging of single microbeads in both upright and inverted configurations suggests that the inverted signal-collection mode can significantly reduce the optical loss, because the optical signal does not need to travel across the microbeads and bulk solution anymore, therefore achieving a 6-fold signal enhancement. This enhancement can translate into an increase of signal-to-noise ratio by 240% in the bead-based ECL immunoassays. The study provides valuable insights into the ECL generation in the bead-based ECL systems and an innovative strategy to enhance the sensitivity of immunoassays through the synergistic integration of single-layer graphene electrodes with an inverted signal-collection mode.

Introduction

Electrochemiluminescence (ECL) is a light emission event induced by electrochemical reactions, possessing unique advantages including low background, high sensitivity and excellent spatiotemporal controllability.[1-4] It has

served as one of the most powerful transduction tools in the in-vitro diagnostics.[5-8] Among various ECL systems, the tris(2,2'-bipyridine)ruthenium(II) ($Ru(bpy)_3^{2+}$)/tri-*n*-propylamine (TPrA) coreactant system is well-established and thought of as the cornerstone of ECL immunoassays, because it has been successfully integrated with immunorecognition for detecting more than 100 disease-related biomarkers and screening new biochemical drugs.[9-13] Despite great success, the ECL immunoassay with a pg/mL sensitivity cannot meet the requirement of detecting low-abundance biomarkers (fg/mL). Continuously increasing the sensitivity of ECL immunoassays therefore is of great significance.

In the commercial microbead-based ECL immunoassay, the light signal originates from the $Ru(bpy)_3^{2+}$ captured on the surface of micrometer-sized magnetic beads through immune and/or biological recognition reactions. In this scheme, the direct electrochemical oxidation of $Ru(bpy)_3^{2+}$ is spatially prohibited,[14-16] and the ECL signal is generated primarily via the so-called low oxidation potential (LOP) pathway, where only TPrA undergoes the electrochemical oxidation at the electrode surface and the generated intermediates, $TPrA^{+\bullet}$ and $TPrA^{\bullet}$, subsequently react with the $Ru(bpy)_3^{2+}$ to form the excited state $Ru(bpy)_3^{2+*}$ that eventually emits the light.[17-19] Metal and carbon are widely used as the electrode materials in the ECL immunoassay, since the electrochemical oxidation of TPrA is kinetically fast on them.[20-22] For example, the commercialized Roche immunoanalyzer use platinum as the electrode material.[9] But the ECL signal of immunoassays can be only collected from the upside of microbeads/electrode, because of the opaqueness of metal and carbon-based electrodes. In other words, the ECL signal mainly generated on the bottom surface of microbeads must be measured from their upside. In this case, the ECL signal suffers from the light scattering by the microbeads and the attenuation due to the partial transparency of the microbeads. Highly transparent and conductive metal oxides (for instance indium tin oxide, ITO) electrodes have been widely deployed in the ECL studies, particularly in ECL imaging, however they are unfit for the ECL immunoassays because of the sluggish electrochemical oxidation kinetics of TPrA on them.[23,24] Although a number of strategies have been elaborated to modify the electrodes to accelerate the electrochemical oxidation of TPrA,[25,26] the potency remains limited. Developing electrodes with both superior electrochemical activities and high transparency is imperative.

On the other hand, unraveling the reaction mechanisms of ECL generation on the microbead surface is also crucial for enhancing the detection sensitivity. Spatially mapping the distribution of ECL intensity on the microbead surface has imparted an interesting approach of elucidating the reaction mechanisms.[27-30] For example, three-dimensional ECL imaging of single polystyrene microbeads labeled with $Ru(bpy)_3^{2+}$ was realized by using an orthogonal side-view microscopy.[31,32] The ECL signal was found to be generated predominantly on the bead surface within a ca. 2–3 μm distance from the electrode, due to the short half-lifetime of $TPrA^{+\bullet}$. The variations of the ECL-emitting distance and the corresponding light intensity profile in the normal direction of the electrode surface over the time were also revealed.[33] Furthermore, by imaging $Ru(bpy)_3^{2+}$-labeled microbeads with diameters ranging from 0.3 μm to 2.8 μm, a highly efficient ECL-generation route near the electrode surface (less than 1 μm) was discovered.[8] Based on the mechanistic understanding of bead-based immunoassays, a variety of novel strategies have been proposed to enhance the ECL generation on the microbead surface to increase the sensitivity, including the use of redox mediators[34,35] and conductive microbeads.[36,37] Another technique of interest is the ECL self-interference spectroscopy (ECLIS), which with a precise spatial resolution allows the measurement of the vertical distribution of ECL intensity in the vicinity of the electrode surface,[38] and so provides insightful information on the reaction mechanisms.[35,39] It certainly holds a great promise for exploring the spatial distribution of the ECL signal on the microbead surface, but heavily impeded by the relatively weak ECL signal generated in this system, due to the poor electrochemical activity of the electrodes available. To be noted that, in this technique, the electrode must have a high transmittance, as the ECL self-interference results from the superposition of the ECL beam emitted directly by the excited-state luminophores and that reflected from the electrode interfaces. At an electrode with only a low light transmittance, the amplitude of reflected ECL beam will be severely attenuated and so the interference between two ECL beams will become ambiguous. A highly transparent and electrochemically active electrode is greatly to be desired in ECLIS.

Single-layer graphene, a two-dimensional carbon material with excellent conductivity, superior mechanical strength, and transparency, has emerged as a revolutionary material for diverse applications.[40-42] Its ability to facilitate the electrochemical oxidation of aliphatic amines also makes it ideal as the substrate electrode for ECL sensing and imaging.[43-45] Moreover, its high transmittance renders also a high ECL collection efficiency. However, in previously reported studies, the use of graphene for mechanistic exploration of ECL processes remains scarce. Here, we integrate single-layer graphene with ECL self-interference spectroscopy and microscopy techniques to investigate and rationalize ECL behavior in bead-based ECL immunoassays.

In this work, we report the preparation of a single-layer graphene-coated ITO electrode, designated as GITO, which exhibits outstanding electrochemical properties and a high transparency, comparable to those of glassy carbon (GC) and ITO electrodes, respectively. First, in comparison with an ITO electrode, the electrochemical oxidation of TPrA at the GITO is significantly accelerated, with an enhancement of approximately 9400-fold. As a result, the ECL intensity of $Ru(bpy)_3^{2+}$ freely diffusing in solution and labeled on the microbead surface is enhanced by 42-fold and 34-fold, respectively. Second, the use of GITO also allows the acquisition of ECL self-interference spectra of $Ru(bpy)_3^{2+}$-labeled microbeads that is infeasible when using other electrode materials. Thus, the spatial distribution of ECL signal on the microbead can be extracted from the ECL self-interference spectrum (as shown in **Scheme 1**, top panel). Moreover, the GITO also allows us to collect the ECL signal and map its spatial distribution on the microbead surface from the electrode underneath (bottom panel, **Scheme 1**). In addition, microscopic imaging of single microbeads in both upright and inverted configurations reveals that collecting the ECL signal from the electrode underneath can markedly reduce the optical loss, as the light signal does not need to travel through the microbeads and the bulk solution anymore, therefore achieving a 6-fold signal enhancement. As a proof-of-concept, bead-based immunoassay was finally performed using GITO as the electrode for the detection of human carcinoembryonic antigen (CEA). Indeed, the signal-to-noise ratio was enhanced by 240% if collecting the ECL signal from the electrode/microbeads underneath, in comparison with the conventional mode of acquiring the signal from the upside.

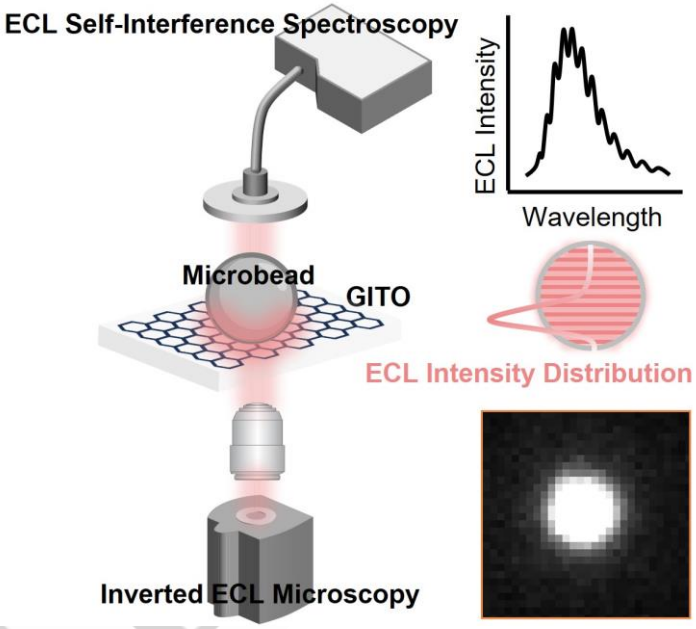

Scheme 1. Schematic of deciphering the ECL generation from a single microbead based on the GITO electrode by ECL self-interference spectroscopy (top) and inverted ECL microscopy (bottom).

Results and Discussion

As shown in **Figure 1a**, a single-layer graphene can be transferred onto the surface of ITO electrodes or other substrates via a wet stripping and transfer method. After coating with graphene, the surface of ITO turns hydrophobic with the water contact angle increased from 41.7° to 91.3° (**Figures 1b** and **1c**). The thickness and roughness of single-layer graphene are 1.55 nm and 1.29 nm, respectively, as determined by atomic force microscope (**Figure 1d**). Due to the ultrathin nature of monolayer graphene, the surface morphology of the GITO electrode remains largely unchanged after graphene transfer (**Figure S1**). Moreover, X-ray photoelectron and Raman spectra also confirm the graphene layer is indeed a monolayer with minimal defects (**Figure S2**). Importantly, as compared in **Figure 1e**, the single-layer graphene has a negligible effect on the transmittance of ITO. Both ITO and GITO exhibit a high transmittance of ca. 90%.

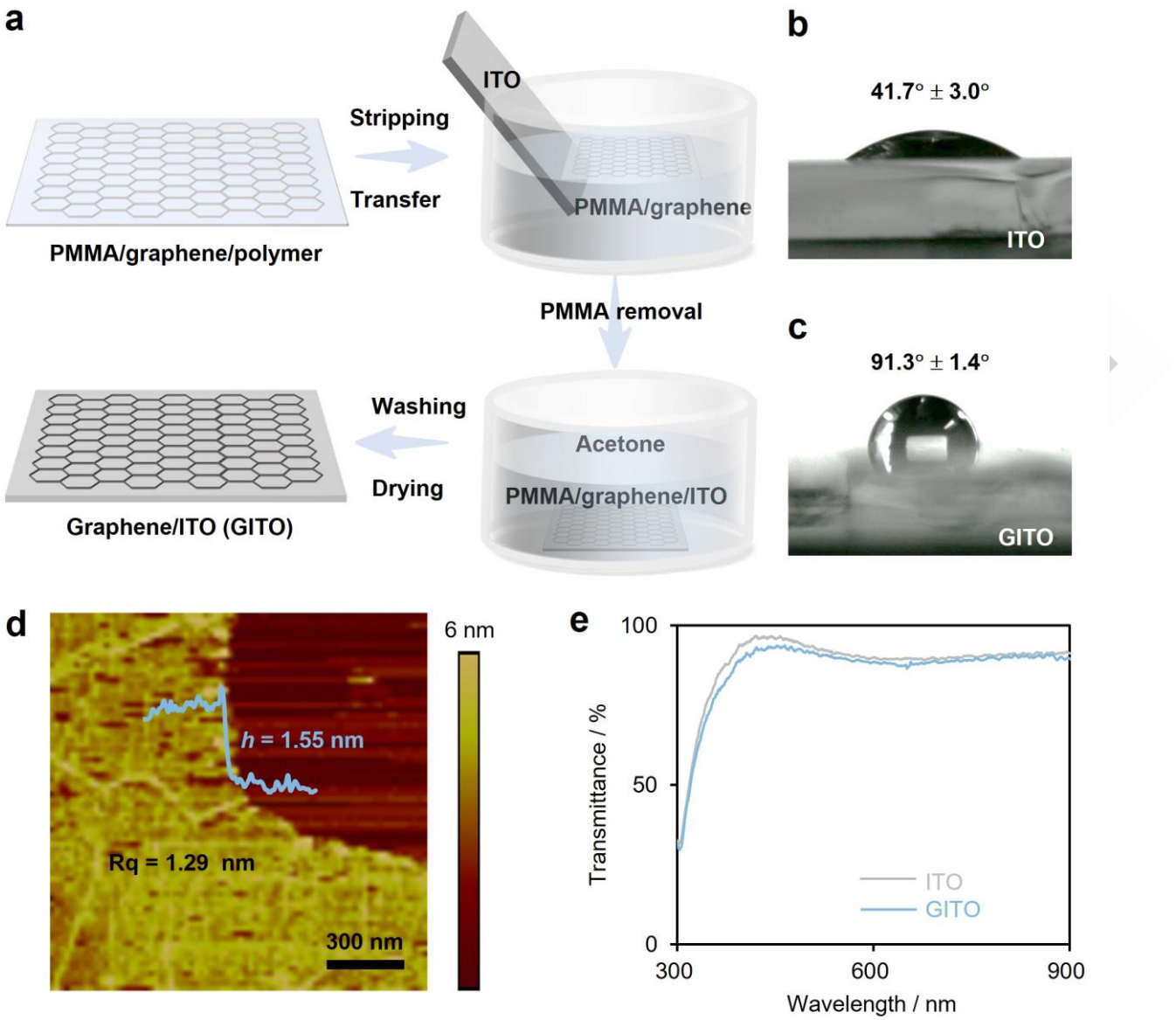

Figure 1. (a) Schematic fabrication of single-layer graphene on planar substrates by the stripping and transfer method. (b, c) Water contact angles of ITO (b) and GITO (c) surfaces. (d) Atomic force microscope (AFM) image of single-layer graphene. (e) UV-visible transmission spectra of ITO and GITO.

The electrochemical property of GITO was also studied. First, the electrochemical oxidation of $Ru(bpy)_3^{2+}$ at both ITO and GITO is kinetically fast, and therefore similar cyclic voltammograms (CVs) are observed (**Figure S3**). While as can be seen from linear scan voltammograms in **Figure 2a**, the electrochemical oxidation of TPrA at the GITO yields a mass-transport controlled current peak, akin to that at a glassy carbon (GC) electrode but noticeably different from the featureless and charge-transfer limited current at the ITO. This peak current is thousand-fold larger than that at an ITO at the same oxidation potentials. To quantitatively compare the performance of three electrodes toward the electrochemical oxidation of TPrA, the standard rate constant (k^0) was further derived according to the Butler–Volmer equation (**Figures S4** and **S5**). As compared in **Figure 2b**, k^0 at the GITO (0.94 $cm{\cdot}s^{-1}$) is indeed comparable to that at the GC (3.1 $cm{\cdot}s^{-1}$), but remarkably larger than that at the ITO (1.0×10^{-4} $cm{\cdot}s^{-1}$). Then, the ECL intensity of $Ru(bpy)_3^{2+}$/TPrA at the GITO was compared with that at the ITO and GC electrodes in the solution containing both 1 μM $Ru(bpy)_3^{2+}$ and 100 mM TPrA. In this condition, the ECL is predominantly generated via the LOP pathway. The ECL intensity at the GITO is a bit (3.6-fold) lower than that at the GC, but much higher than that at the ITO by 42-fold (**Figures 2c** and **2d**).

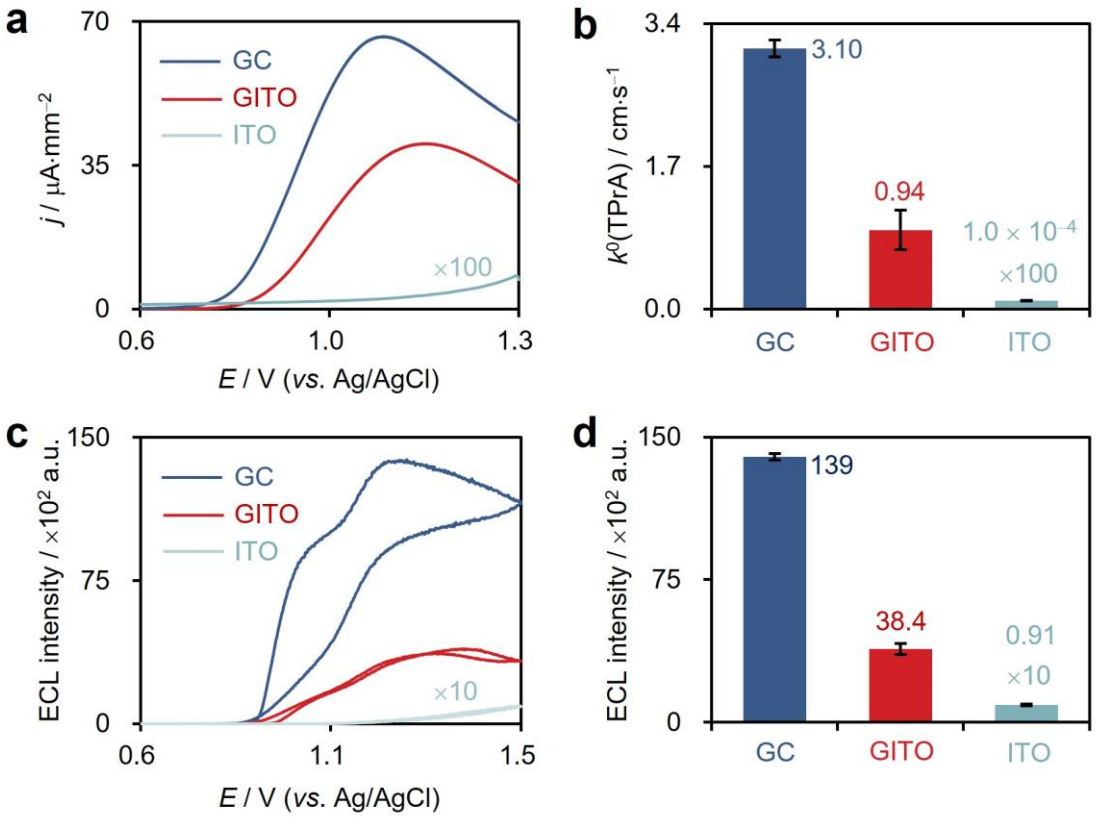

Figure 2. (a) Linear sweep voltammograms obtained at the GC, GITO and ITO electrodes in phosphate buffer (PB) solution (0.2 M, pH 7.4) with 100 mM TPrA. (b) k^0 of TPrA electrochemical oxidation on the three electrodes. The magnitudes of j and k^0 obtained at the ITO are multiplied by 100 for comparison. (c, d) ECL intensity-potential curves (c) and maximum intensities (d) measured at the three electrodes in 0.2 M PB solution (pH 7.4) containing both 1 μM $Ru(bpy)_3^{2+}$ and 100 mM TPrA. The ECL intensity at the ITO is 10-fold magnified for comparison.

Above results imply the great potential of GITO in mapping the distribution of ECL signal on the microbead surface. This information will be of great significance for optimizing the immunoassay sensitivity. However, spatial mapping of the ECL signal distribution on the microbead surface is so far exclusively based on the ECL imaging.[27-29] Although ECLIS has been well deployed to map the distribution of ECL signal generated by freely diffusing $Ru(bpy)_3^{2+}$ in solution,[35,39] it remains very difficult to record a well-defined ECL self-interference spectrum for the $Ru(bpy)_3^{2+}$ immobilized on microbeads using previously developed ITO or Au electrode. Indeed, these electrodes can only provide a weak ECL signal (limited by the slow electrochemical oxidation kinetics of TPrA) and a deficient transmittance (for Au electrode). Given the GITO possesses both superior electrochemical activities and a high transmittance, it can principally serve as an ideal electrode for ECLIS measurements. Therefore, using the above-mentioned method, single-layer graphene coated ITO/silica/silicon (GITO/SiO_2/Si) electrode was prepared by transferring the single-layer graphene onto the custom ITO/SiO_2/Si electrode, which consists of 102-nm-thick ITO and 6.05-μm-thick SiO_2 deposited on the silicon substrate (**Figure S6**). As proved by the white-light interferometry, the optical interferometric peaks in the wavelength range of 600 ~ 800 nm are nearly unchanged before and after the graphene transfer (**Figures 3a** and **3b**). Furthermore, the interferometric amplitude (namely the deviation between the interferometric spectrum and its envelope) of the GITO/SiO_2/Si is very close to that of the ITO/SiO_2/Si, but much larger than that of the Au/SiO_2/Si (**Figure S7**). So, it follows that the single-layer graphene does not affect the light interference thanks to its high transparency and that the GITO/SiO_2/Si is indeed more suitable as the substrate electrode for ECLIS.

$Ru(bpy)_3^{2+}$-labeled polystyrene microbeads (Ru-PSBs) that can mimic immunobeads were prepared by subjecting amino-functionalized PSBs with a diameter of 3.8 μm to an amide reaction with bis(2,2'-bipyridyl)(4-carboxypropyl-2,2'-bipyridyl)ruthenium(II). The successful attachment of $Ru(bpy)_3^{2+}$ to the surface of PSBs was confirmed by their bright photoluminescence (**Figure S8**). Subsequently, a single-layer of Ru-PSBs was prepared by drop-casting the suspension containing Ru-PSBs on the electrode surface to measure the ECL self-interference spectra (**Figure S9**). As shown in **Figure 3c**, the ECL self-interference results from the superposition of two ECL beams, one of which is emitted directly from the surface of Ru-PSBs. The other travels across the layer of Ru-PSBs and is then

reflected at the interfaces of GITO/SiO_2/Si electrode. It should be noted that only ill-defined ECL self-interference spectra were acquired for Ru-PSBs, if using ITO/SiO_2/Si and Au/SiO_2/Si electrodes (**Figure S10**). In contrast, the ECL self-interference spectrum was successfully obtained using the GITO/SiO_2/Si electrode (**Figure 3d**), though the amplitude of ECL self-interference spectrum of Ru-PSBs is much smaller than that of freely diffusing $Ru(bpy)_3^{2+}$ (**Figure S11**). This decrease can be largely ascribed to the relatively low transmittance of PSBs (**Figure S12**), causing a substantial attenuation of reflected ECL beam and thereby reducing the interference of two ECL beams.

To rationalize the generation of ECL self-interference for Ru-PSBs and to calculate the thickness/position of ECL-emitting layer, a microbead-based self-interference model was established (see **Section S3.7**, **Figures S13** and **S14** in supporting information for details). Briefly, the ECL signal generated on the surface of Ru-PSBs was divided into a number of sublayers along the normal direction of the electrode surface (**Figure 3e**). The ECL self-interference spectrum of each sublayer was calculated by the MATLAB software, and the superposition of all the sublayer spectra yielded a theoretical ECL self-interference spectrum. When this theoretical spectrum best matching with that recorded experimentally (**Figure 3f**), the position/height of the highest sublayer is defined as the thickness of the ECL-emitting layer. In this way, the thickness of ECL-emitting layer on Ru-PSBs obtained by ECLIS is 770 ± 60 nm.

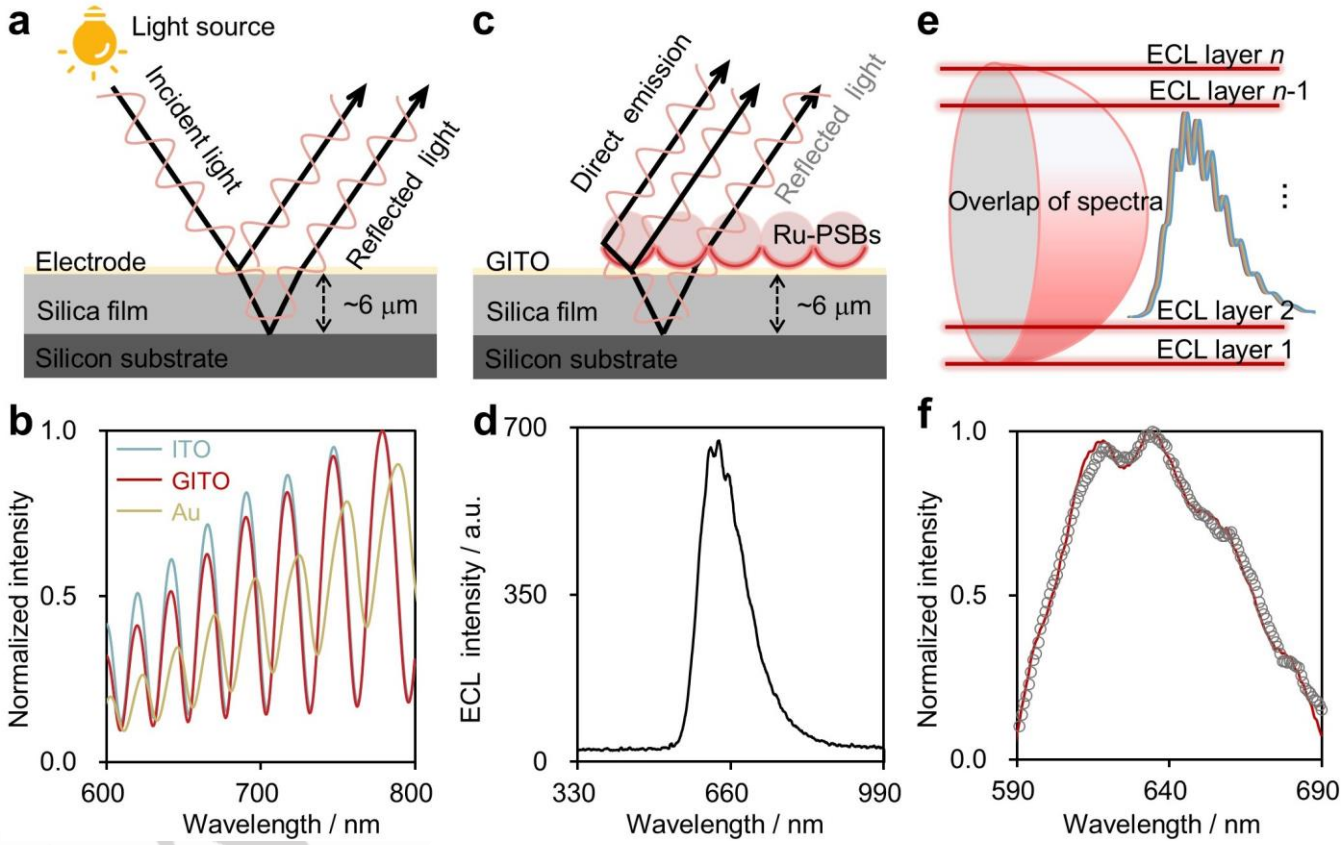

Figure 3. (a) Schematic principle of the white light interferometry. (b) Normalized white light interferometric spectra at the ITO/SiO_2/Si (blue), GITO/SiO_2/Si (red) and Au/SiO_2/Si (yellow) electrodes. (c) Schematic of the ECL self-interference of Ru-PSBs. (d) ECL self-interference spectrum of single-layer Ru-PSBs on the GITO/SiO_2/Si electrode obtained in 0.2 M PB solution (pH 7.4) containing 100 mM TPrA. The applied potential was +1.5 V (*vs.* Ag/AgCl) and the spectral integration time was 2 s. (e) Schematic of calculating the thickness of the ECL-emitting layer on a single Ru-PSB. (f) Normalized experimental (solid red line) and theoretical (open circles) ECL self-interference spectra of Ru-PSBs.

Subsequently, ECL imaging was employed to further investigate the ECL distribution on the surface of individual Ru-PSBs. First, ECL generation by individual Ru-PSBs on the ITO, GITO, and GC electrodes was comparatively studied by imaging single Ru-PSBs using an upright microscope (upright configuration, **Scheme 2**). As shown in **Figures 4a** and **S15**, compared with an ITO, the ECL intensity of single Ru-PSBs on the GITO is enhanced by 34-fold, although it is still 2-3 times lower than that on the GC electrode. The lower ECL intensity compared to the GC electrode can be attributed to residual polymeric contaminants (e.g., PMMA), which partially obstruct electroactive sites on the GITO surface and thus impede the electron transfer. Moreover, thanks to the high transparency of the GITO, the ECL images of single Ru-PSBs can be also recorded from the underneath of GITO by using an inverted

microscope (inverted configuration, **Scheme 2**). It is very interesting to see that the ECL intensity of single Ru-PSBs is enhanced by 6-fold in comparison with that in the upright mode (**Figure 4b**). Apart from the difference in optics, such as optical path and objective lens used, between these two imaging configurations, this enhancement can be connected with the significant reduction of the light loss arising from the light scattering and attenuation by partially opaque PSBs and in solution. On the other hand, the ECL area of Ru-PSBs is also decreased by 52% when switching from the upright to the inverted configuration (**Figures 4b-f** and **S16**). This decrease can be ascribed to the dramatic decline of ECL intensity on the microbead surface with increasing the distance from the electrode surface, since most of ECL photons are emitted from the bottom surface of the microbead via the so-called LOP route. In this case, in the upright configuration where the objective lens is placed on the upside of Ru-PSBs, most of ECL photons must travel across the microbead and solution, leading to the overestimation of ECL area due to the multiple refractions and scattering of ECL at the microbead-solution interface (**Figure S17**). In contrast, in the inverted imaging configuration where the objective is placed beneath the Ru-PSBs, the ECL photons can be directly and efficiently collected (**Figure S17**).The results suggest that collecting the ECL signal from the underneath of Ru-PSBs can not only minimize the loss of optical signal due to partially opaque microbeads and in solution, but also reduce the error in determining the ECL area of single Ru-PSBs by obviating the effects of scattering, reflection and refraction.

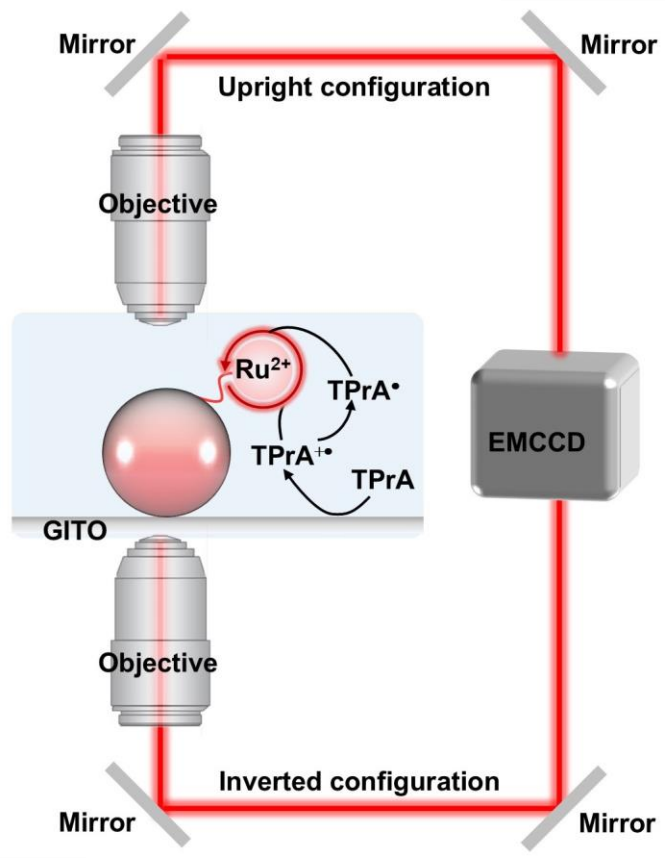

Scheme 2. Schematic of ECL microscope for capturing the ECL images of single Ru-PSBs under the upright (top) and inverted (bottom) imaging configurations.

To rationalize the variations of ECL intensity and ECL area of single Ru-PSBs in two imaging configurations, finite element simulations were performed. First, the distribution of ECL intensity on a single Ru-PSB surface was calculated using the COMSOL Multiphysics software (see **Section S5**, **Figure S18** and **Tables S1-S5** in supporting information for details). Since it is difficult to take into account the optical effects of microbead and electrode in the finite element simulations, there is a discrepancy between calculated and experimentally captured ECL images (**Figure S19**). So, optical simulations (see details in **Section S6** in supporting information file) based on the discrete dipole approximation were further conducted to reconstruct the spatial distribution of the ECL intensity on the microbead surface.[46-49] In the optical simulations, the parameters of the lens, including the magnification and numerical aperture, were considered for the two configurations, excluding the error due to the light collection efficiency of lens and allowing a reliable evaluation of the impact of acquisition mode on the ECL intensity of Ru-

PSBs. As shown in **Figures 4g** and **4h**, the calculated ECL image of a Ru-PSB in the inverted configuration shows a much brighter light emitting spot than that in the upright configuration, consistent with the experimental results, confirming that the detection in the inverted configuration can indeed increase the collection efficiency of ECL photons emitted by Ru-PSBs. However, the simulation results also identify a decrease of ECL intensity at the radial center of the microbead, being different than the experimental images (**Figure S20**). The difference is most likely associated with the omission of multiple light reflections and refractions at the microbead-solution interface in the simulations. Nevertheless, the ECL images obtained in the inverted configuration can more accurately reflect the distribution of ECL intensity on the microbead surface. As displayed in **Figure S21**, the thickness of ECL-emitting layer on Ru-PSBs is estimated to be 1130 ± 140 nm according to the ECL area in the inverted image, which is a bit larger than that obtained from ECLIS. The discrepancy is likely connected with a relatively low photon collection efficiency of the fiber optic spectrometer compared with the electron multiplying charge coupled device (EMCCD) camera, so limiting its ability to register weak light emitted at a large distance from the electrode surface. Therefore, a combination of ECLIS and ECL imaging enables an accurate analysis of the ECL generation by Ru-PSBs, offering valuable insights into the reaction mechanisms for improving the performance of microbead-based ECL immunoassays.

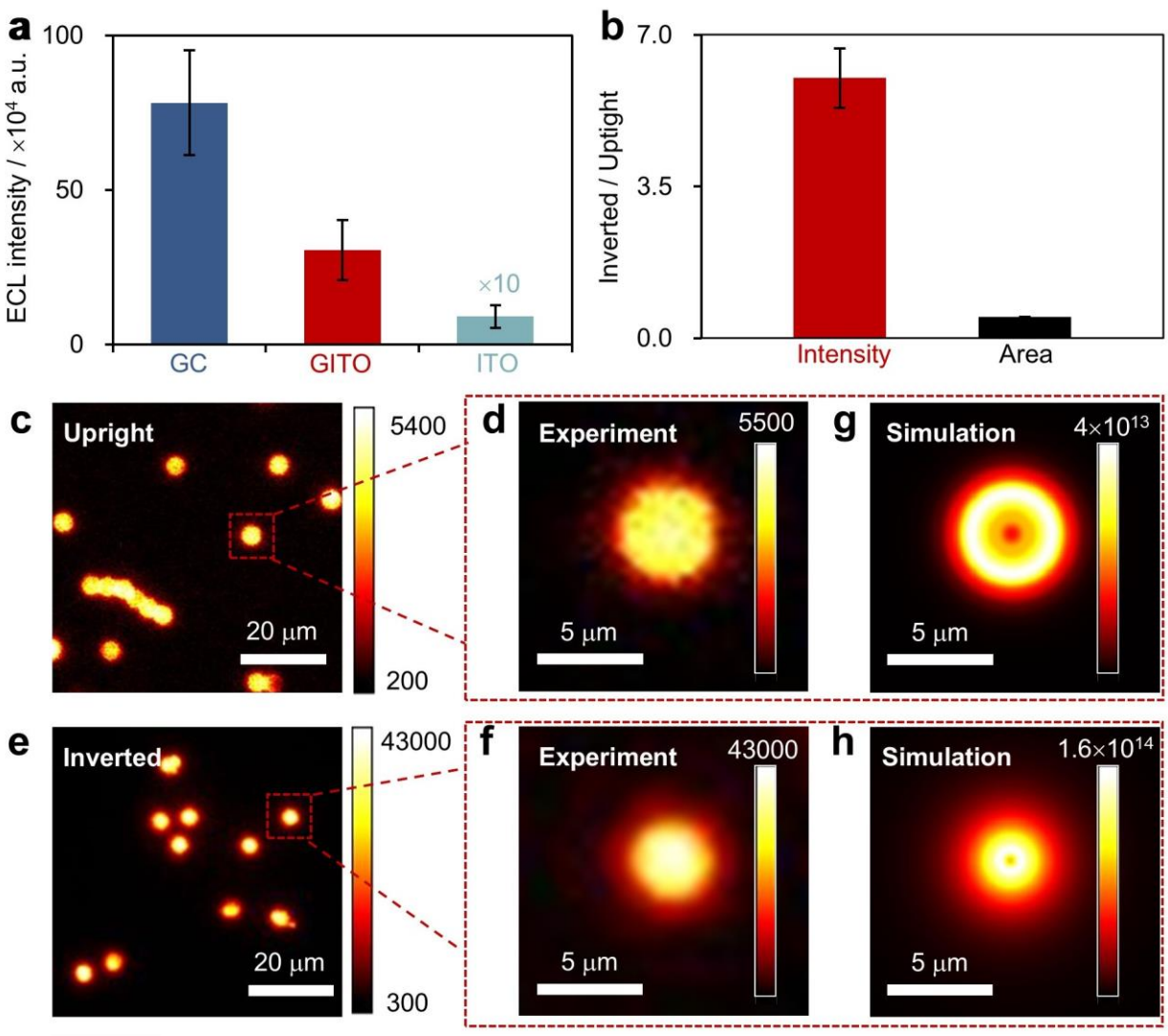

Figure 4. (a) The ECL intensity of single Ru-PSBs on different electrodes using the upright configuration. (b) The relative ECL intensity and ECL area of single Ru-PSBs obtained using the upright and inverted configurations. The data represents the statistical counting of 100 single beads. (c-f) ECL images of Ru-PSBs experimentally captured in the upright (c, d) and inverted (e, f) configurations. (g, h) Simulated ECL images of a single bead in the upright (g) and inverted (h) configurations.

As demonstrated above, collecting the ECL signal from the bottom of electrode/microbeads can enhance the collected intensity of signal and potentially increase the sensitivity of microbead-based immunoassay. So, an ECL immunoassay was comparatively conducted for the detection of CEA, as shown in **Figure 5a**, under two signal

collection configurations, namely the bottom generation-bottom collection (BG-BC) and bottom generation-top collection (BG-TC) modes. First, CEA, $Ru(bpy)_3^{2+}$-conjugated detection antibody and biotin-labeled capture antibody were incubated in a phosphate buffer saline (PBS) to form the immunocomplexes, which were then captured onto the streptavidin-labeled magnetic microbeads. Subsequently, the beads were separated, washed and immobilized on the GITO electrode surface via a permanent magnet (**Figure S22a**). Finally, the ECL signal was collected under the BG-BC and BG-TC configurations, using a photomultiplier tube (PMT) as the detector (**Figures 5a** and **S22b**). As displayed in **Figure 5b**, the ECL signal collected in the BG-BC mode is indeed higher than that in the other mode, with an approximately 2.4-fold increase in the signal-to-noise ratio (S/N). The improved SNR is anticipated to significantly enhance the analytical sensitivity, facilitating the detection of low-abundance targets.[50-52]

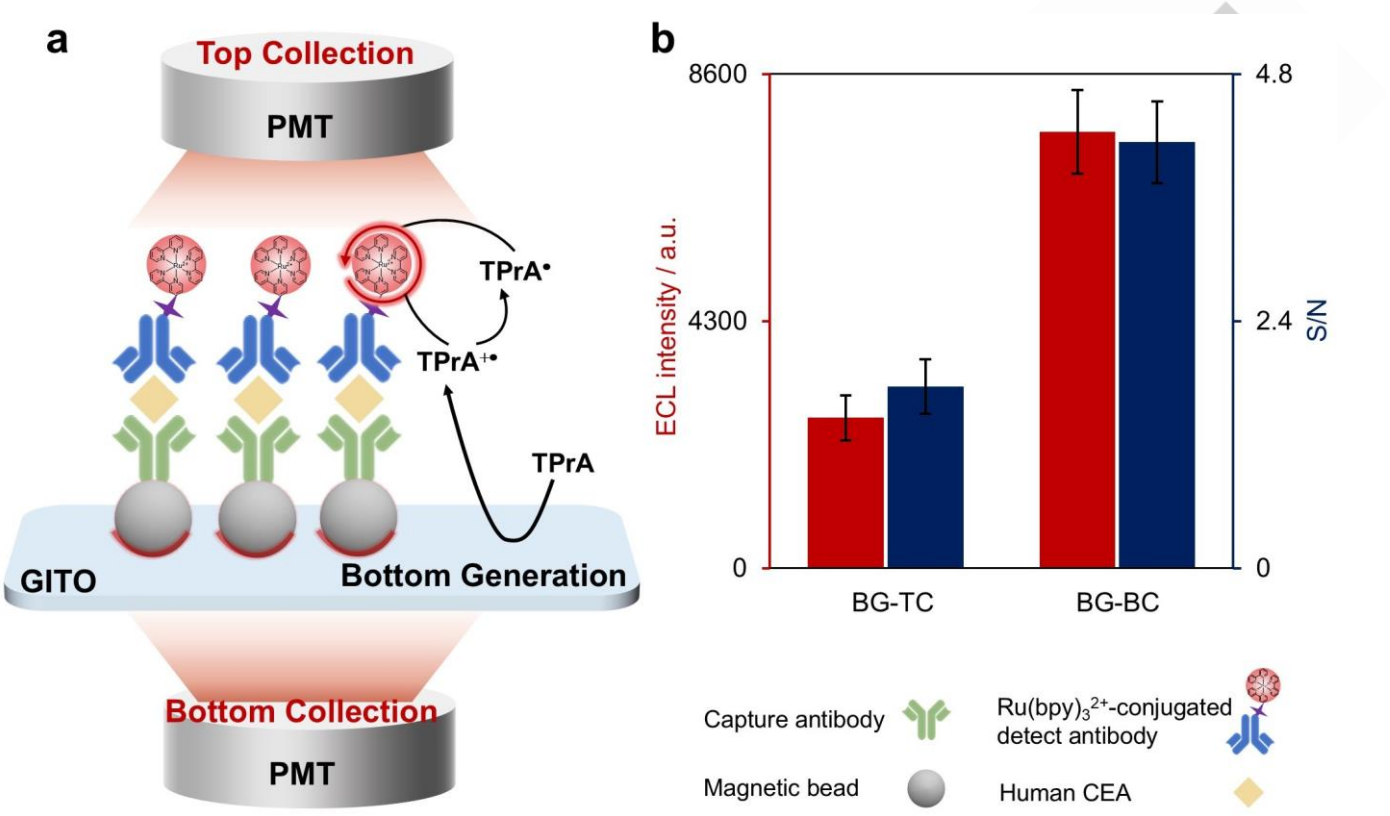

Figure 5. (a) Schematic of the BG-TC and BG-BC modes for microbead-based ECL immunoassays. (b) ECL intensity (red) and the signal-to-noise ratio (S/N, blue) of the immunoassay recorded in 0.2 M PB solution (pH 7.4) with 100 mM TPrA. The concentration of CEA was 25 ng·mL^{-1} and the applied potential was +1.5 V (*vs.* Ag/AgCl). Standard deviation, n = 3.

Conclusion

In summary, transparent single-layer graphene electrodes combining the outstanding electrochemical properties with the high optical transmittance were fabricated and used to unravel the ECL generation in the microbead system and enhance its performance. The superior electrochemical activity of GITO promotes the electrochemical oxidation of TPrA by 9400-fold in comparison with the pristine ITO, leading to a 34-fold enhancement in the ECL intensity of Ru-PSBs. Moreover, the high transparency of GITO enables the spatially-resolved measurement of the distribution of ECL signal on Ru-PSBs, with an ECL-emitting layer thickness determined to be 770 ± 60 nm and 1130 ± 140 nm by ECLIS and inverted ECL imaging, respectively. In addition, as proved by ECL imaging of single Ru-PSBs in the upright and inverted configurations, the ECL signal can be enhanced by up to 6-fold when collecting the signal from the electrode/microbead underneath rather than from the upside, because the optical loss caused by propagation of light through the microbeads and solution is remarkably decreased. Finally, based on this strategy, the signal-to-noise ratio of microbead-based ECL immunoassay can be enhanced by 240%. The results demonstrate the versatility of single-layer graphene electrodes and their merits for applications in ECL spectroscopy, microscopic imaging and ultrasensitive ECL bioassays. We are using the transparent single-layer graphene electrode, in conjunction with nanostructured luminophores, to detect low-abundance biomarkers, and the results will be reported soon later elsewhere.

Acknowledgements

This work is financially supported by the National Natural Science Foundation of China (22125405, 22204142) and the ANR (MAPICS-ANR-23-CE42-0018-02). The authors would like to thank Mrs. Fang Chen (Chemistry Instrumentation Center of the Chemistry Department) for technical assistance with SEM measurements, Mrs. Chen Chen (Chemistry Instrumentation Center of the Chemistry Department) for her help on Raman measurement and analysis, and Dr. Yangfan Lu (School of Materials Science and Engineering) for her help on XPS measurement and analysis.

Keywords: electrochemiluminescence • single-layer graphene • microbead-based immunoassays • inverted imaging • self-interference spectroscopy

[1] M. Hesari, Z. Ding, Review—Electrogenerated Chemiluminescence: Light Years Ahead. *J. Electrochem. Soc.* **2015**, *163*, H3116.

[2] L. Hu, G. Xu, Applications and Trends in Electrochemiluminescence. *Chem. Soc. Rev.* **2010**, *39*, 3275.

[3] G. Valenti, E. Rampazzo, S. Kesarkar, D. Genovese, A. Fiorani, A. Zanut, F. Palomba, M. Marcaccio, F. Paolucci, L. Prodi, Electrogenerated Chemiluminescence from Metal Complexes-Based Nanoparticles for Highly Sensitive Sensors Applications. *Coord. Chem. Rev.* **2018**, *367*, 65.

[4] Z. Liu, W. Qi, G. Xu, Recent Advances in Electrochemiluminescence. *Chem. Soc. Rev.* **2015**, *44*, 3117.

[5] F. Du, Y. Chen, C. Meng, B. Lou, W. Zhang, G. Xu, Recent Advances in Electrochemiluminescence Immunoassay Based on Multiple-Signal Strategy. *Curr. Opin. Electrochem.* **2021**, *28*, 100725.

[6] L. Yang, J. Li, Recent Advances in Electrochemiluminescence Emitters for Biosensing and Imaging of Protein Biomarkers. *Chemosensors* **2023**, *11*, 432.

[7] A. Chen, W. Liang, H. Wang, Y. Zhuo, Y. Chai, R. Yuan, Anodic Electrochemiluminescence of Carbon Dots Promoted by Nitrogen Doping and Application to Rapid Cancer Cell Detection. *Anal. Chem.* **2020**, *92*, 1379.

[8] A. Zanut, A. Fiorani, S. Canola, T. Saito, N. Ziebart, S. Rapino, S. Rebeccani, A. Barbon, T. Irie, H.-P. Josel, F. Negri, M. Marcaccio, M. Windfuhr, K. Imai, G. Valenti, F. Paolucci, Insights into the Mechanism of Coreactant Electrochemiluminescence Facilitating Enhanced Bioanalytical Performance. *Nat. Commun.* **2020**, *11*, 2668.

[9] N. Sojic, in *Analytical Electrogenerated Chemiluminescence: From Fundamentals to Bioassays, Vol. 15* (Ed.: N. Sojic), The Royal Society of Chemistry, **2020**, pp. 433-469.

[10] F. Deiss, C. N. LaFratta, M. Symer, T. M. Blicharz, N. Sojic, D. R. Walt, Multiplexed Sandwich Immunoassays Using Electrochemiluminescence Imaging Resolved at the Single Bead Level. *J. Am. Chem. Soc.* **2009**, *131*, 6088.

[11] W. Guo, H. Ding, C. Gu, Y. Liu, X. Jiang, B. Su, Y. Shao, Potential-Resolved Multicolor Electrochemiluminescence for Multiplex Immunoassay in a Single Sample. *J. Am. Chem. Soc.* **2018**, *140*, 15904.

[12] M. Sornambigai, L. Bouffier, N. Sojic, S. S. Kumar, Tris(2,2'-bipyridyl)ruthenium (II) Complex as a Universal Reagent for the Fabrication of Heterogeneous Electrochemiluminescence Platforms and Its Recent Analytical Applications. *Anal. Bioanal. Chem.* **2023**, *415*, 5875.

[13] A. Barhoum, Z. Altintas, K. S. S. Devi, R. J. Forster, Electrochemiluminescence Biosensors for Detection of Cancer Biomarkers in Biofluids: Principles, Opportunities, and Challenges. *Nano Today* **2023**, *50*, 101874.

[14] L. S. Dolci, S. Zanarini, L. D. Ciana, F. Paolucci, A. Roda, Development of a New Device for Ultrasensitive Electrochemiluminescence Microscopy Imaging. *Anal. Chem.* **2009**, *81*, 6234.

[15] W. Zhu, J. Dong, G. Ruan, Y. Zhou, J. Feng, Quantitative Single-Molecule Electrochemiluminescence Bioassay. *Angew. Chem. Int. Ed.* **2023**, *62*, e202214419.

[16] W. Fu, X. Wang, X. Ying, T. Sun, Y. Wang, J. Wang, B. Su, Electrochemiluminescence Lateral Flow Immunoassay Using Ruthenium(II) Complex-Loaded Dendritic Mesoporous Silica Nanospheres for Highly Sensitive and Quantitative Detection of SARS-CoV-2 Nucleocapsid Protein. *Adv. Funct. Mater.* **2024**, *34*, 2409632.

[17] W. J. Miao, J. P. Choi, A. J. Bard, Electrogenerated Chemiluminescence 69: The Tris(2,2'-bipyridine)ruthenium(II), ($Ru(Bpy)_3^{2+}$)/Tri-*n*-propylamine (TPrA) System Revisited-a New Route Involving $TPrA^{\bullet+}$ Cation Radicals. *J. Am. Chem. Soc.* **2002**, *124*, 14478.

[18] X. Huang, B. Li, Y. Lu, Y. Liu, S. Wang, N. Sojic, D. Jiang, B. Liu, Direct Visualization of Nanoconfinement Effect on Nanoreactor via Electrochemiluminescence Microscopy. *Angew. Chem. Int. Ed.* **2023**, *62*, e202215078.

[19] A. Zanut, F. Palomba, M. Rossi Scota, S. Rebeccani, M. Marcaccio, D. Genovese, E. Rampazzo, G. Valenti, F. Paolucci, L. Prodi, Dye-Doped Silica Nanoparticles for Enhanced ECL-Based Immunoassay Analytical Performance. *Angew. Chem. Int. Ed.* **2020**, *59*, 21858.

[20] G. Valenti, A. Fiorani, H. Li, N. Sojic, F. Paolucci, Essential Role of Electrode Materials in Electrochemiluminescence Applications. *ChemElectroChem* **2016**, *3*, 1990.

[21] X.-H. Xu, A. J. Bard, Electrogenerated Chemiluminescence. 55. Emission from Adsorbed $Ru(bpy)_3^{2+}$ on Graphite, Platinum, and Gold. *Langmuir* **1994**, *10*, 2409.

[22] S. Parveen, Y. Chen, Y. Yuan, L. Hu, W. Zhang, M. R. H. S. Gilani, Y. Shi, R. Aziz ur, G. Xu, Electrochemiluminescence of $[Ru(bpy)_3]^{2+}$/Tripropylamine at Glassy Carbon, Platinum, and Palladium Electrodes. *Sens. Actuators Rep.* **2021**, *3*, 100062.

[23] T. Li, J. Ding, Y. Wang, B. Su, Regulating the Work Function and Surface Hydrophobicity of an Indium Tin Oxide Electrode for Enhanced Electrochemiluminescence Analysis. *Chem. Commun.* **2024**, *60*, 15007.

[24] J. Ding, P. Zhou, B. Su, Quantum Efficiency of Electrochemiluminescence Generation by Tris(2,2'-bipyridine)ruthenium(II) and Tri-*n*-propylamine Revisited from a Kinetic Reaction Model. *ChemElectroChem* **2022**, *9*, e202200236.

[25] R. Huang, M.-Y. Wei, L.-H. Guo, Enhanced Electrogenerated Chemiluminescence of $Ru(Bpy)_3^{2+}$/Tripropylamine System on Indium Tin Oxide Nanoparticle Modified Transparent Electrode. *J. Electroanal. Chem.* **2011**, *656*, 136.

[26] F.-R. F. Fan, A. J. Bard, Observing Single Nanoparticle Collisions by Electrogenerated Chemiluminescence Amplification. *Nano Lett.* **2008**, *8*, 1746.

[27] P. Dutta, D. Han, B. Goudeau, D. Jiang, D. Fang, N. Sojic, Reactivity Mapping of Luminescence in Space: Insights into Heterogeneous Electrochemiluminescence Bioassays. *Biosens. Bioelectron.* **2020**, *165*, 112372.

[28] Y. Feng, W. Zhou, X. Wang, J. Zhang, M. Zou, C. Zhang, H. Qi, Imaging and Simulation of Ruthenium Derivative Coating Microbeads at the Opaque Electrode with Electrogenerated Chemiluminescence. *Chem. Biomed. Imaging* **2023**, *1*, 648.

[29] Y. Wang, B. Su, Deciphering the Mechanisms of Electrochemiluminescence by Spatially Resolved Measurements. *Anal. Sens.* **2021**, *1*, 148.

[30] Y. Feng, C. Wang, W. Zhou, X. Yang, F. Paolucci, G. Valenti, H. Qi, Tomography Electrogenerated Chemiluminescence Imaging from Magnetic Microbeads. *Small* **2025**, *21*, 2500804.

[31] M. Sentic, M. Milutinovic, F. Kanoufi, D. Manojlovic, S. Arbault, N. Sojic, Mapping Electrogenerated Chemiluminescence Reactivity in Space: Mechanistic Insight into Model Systems Used in Immunoassays. *Chem. Sci.* **2014**, *5*, 2568.

[32] A. Fiorani, D. Han, D. Jiang, D. Fang, F. Paolucci, N. Sojic, G. Valenti, Spatially Resolved Electrochemiluminescence through a Chemical Lens. *Chem. Sci.* **2020**, *11*, 10496.

[33] D. Han, D. Fang, G. Valenti, F. Paolucci, F. Kanoufi, D. Jiang, N. Sojic, Dynamic Mapping of Electrochemiluminescence Reactivity in Space: Application to Bead-Based Assays. *Anal. Chem.* **2023**, *95*, 15700.

[34] A. Fracassa, C. I. Santo, E. Kerr, S. Knežević, D. J. Hayne, P. S. Francis, F. Kanoufi, N. Sojic, F. Paolucci, G. Valenti, Redox-Mediated Electrochemiluminescence Enhancement for Bead-Based Immunoassay. *Chem. Sci.* **2024**, *15*, 1150.

[35] N. S. Adamson, S. J. Blom, E. H. Doeven, T. U. Connell, C. Hadden, S. Knežević, N. Sojic, A. Fracassa, G. Valenti, F. Paolucci, J. Ding, Y. Wang, B. Su, C. Hua, P. S. Francis, Electrochemiluminescence Enhanced by a Non-Emissive Dual Redox Mediator. *Angew. Chem. Int. Ed.* **2024**, *63*, e202412097.

[36] X. Yang, J. Hang, W. Qu, Y. Wang, L. Wang, P. Zhou, H. Ding, B. Su, J. Lei, W. Guo, Z. Dai, Gold Microbeads Enabled Proximity Electrochemiluminescence for Highly Sensitive and Size-Encoded Multiplex Immunoassays. *J. Am. Chem. Soc.* **2023**, *145*, 16026.

[37] S. Rebeccani, C. Wetzl, V. A. Zamolo, A. Criado, G. Valenti, F. Paolucci, M. Prato, Electrochemiluminescent Immunoassay Enhancement Driven by Carbon Nanotubes. *Chem. Commun.* **2021**, *57*, 9672.

[38] Y. Wang, W. Guo, Q. Yang, B. Su, Electrochemiluminescence Self-Interference Spectroscopy with Vertical Nanoscale Resolution. *J. Am. Chem. Soc.* **2020**, *142*, 1222.

[39] Y. Wang, J. Ding, P. Zhou, J. Liu, Z. Qiao, K. Yu, J. Jiang, B. Su, Electrochemiluminescence Distance and Reactivity of Coreactants Determine the Sensitivity of Bead-Based Immunoassays. *Angew. Chem. Int. Ed.* **2023**, *62*, e202216525.

[40] W. Nan, J. Lin, L. Xu, L. Han, D. Zhan, Modulating the Interfacial Electrochemical Behavior of Single Layer Graphene. *Curr. Opin. Electrochem.* **2025**, *49*, 101608.

[41] K. S. Novoselov, A. K. Geim, S. V. Morozov, D. Jiang, Y. Zhang, S. V. Dubonos, I. V. Grigorieva, A. A. Firsov, Electric Field Effect in Atomically Thin Carbon Films. *Science* **2004**, *306*, 666.

[42] W. Li, M. Wojcik, K. Xu, Optical Microscopy Unveils Rapid, Reversible Electrochemical Oxidation and Reduction of Graphene. *Nano Lett.* **2019**, *19*, 983.

[43] T. Watanabe, R. Ishikawa, N. Hara, T. Iwasaki, M. Miyachi, Y. Shiigi, M. Takahashi, D. Kuroki, S. Koh, Single-Layer Graphene as a Transparent Electrode for Electrogenerated Chemiluminescence Biosensing. *Electrochem. Commun.* **2022**, *138*, 107290.

[44] E. K. Walker, D. A. Vanden Bout, K. J. Stevenson, Carbon Optically Transparent Electrodes for Electrogenerated Chemiluminescence. *Langmuir* **2012**, *28*, 1604.

[45] G. Valenti, M. Zangheri, S. E. Sansaloni, M. Mirasoli, A. Penicaud, A. Roda, F. Paolucci, Transparent Carbon Nanotube Network for Efficient Electrochemiluminescence Devices. *Chem. Eur. J* **2015**, *21*, 12640.

[46] D. Han, D. Jiang, G. Valenti, F. Paolucci, F. Kanoufi, P. C. Chaumet, D. Fang, N. Sojic, Optics Determines the Electrochemiluminescence Signal of Bead-Based Immunoassays. *ACS Sens.* **2023**, *8*, 4782.

[47] P. C. Chaumet, The Discrete Dipole Approximation: A Review. *Mathematics* **2022**, *10*, 3049.

[48] P. C. Chaumet, T. Zhang, A. Sentenac, Fast Far-Field Calculation in the Discrete Dipole Approximation. *J. Quant. Spectrosc. Radiat. Transf.* **2015**, *165*, 88.

[49] L. Oliveira, W. H. Campos, M. S. Rocha, Optical Trapping and Manipulation of Superparamagnetic Beads Using Annular-Shaped Beams. *Methods Protoc.* **2018**, *1*, 44.

[50] R. R. Williams, Fundamental Limitations on the Use and Comparison of Signal-to-Noise Ratios. *Anal. Chem.* **1991**, *63*, 1638.

[51] X. Liu, S. Zhao, Y. Xu, B. Zhang, J. Huang, F. Liu, N. Yang, W. Lu, D. Shi, D. Xie, Y. Hou, G. Wang, A Novel High-Throughput and Sensitive Electrochemiluminescence Immunoassay System. *Bioengineering* **2024**, *11*, 885.

[52] M. M. Sanagi, S. L. Ling, Z. Nasir, D. Hermawan, W. A. Wan Ibrahim, A. A. Naim, Comparison of Signal-to-Noise, Blank Determination, and Linear Regression Methods for the Estimation of Detection and Quantification Limits for Volatile Organic Compounds by Gas Chromatography. *J AOAC Int.* **2009**, *92*, 1833.